Petroleum Science 22 (2025) 4462–4491

Contents lists available at ScienceDirect

Petroleum Science

journal homepage: www.keaipublishing.com/en/journals/petroleum-science

A modeling-inversion methodology for source rocks based on clay-kerogen lamination and pore geometry

Cong Luo[a], Jun-Wei Cheng[a], Jing Ba[a,*], José Carcione[a,b], Lu-Lu Chen[a]

[a] *School of Earth Sciences and Engineering, Hohai University, Nanjing, 211100, Jiangsu, China*
[b] *National Institute of Oceanography and Applied Geophysics – OGS, Trieste, 34010, Italy*

ARTICLE INFO

Article history:
Received 21 November 2024
Received in revised form
18 May 2025
Accepted 30 June 2025
Available online 5 July 2025

Edited by Meng-Jiao Zhou

Keywords:
Rock physics modeling
Source rocks
Connectivity index
Pore aspect ratio
Lamination index
VTI anisotropy

ABSTRACT

Source rocks (shales) exhibit different geometric pore types and considerable anisotropy caused by the preferential orientation of the clay and kerogen layers, which is not accounted for in classical rock-physics models. Pore geometry can be effectively studied through the aspect ratio, and in this study, we use the aspect ratio to characterize different pore geometries. Then, we consider a pore connectivity index as well as a lamination index associated with these orientations. An inclusion-based theory (differential effective medium and self-consistent approximation) and the Brown-Korringa equations are used in the modeling approach. The results show that the indices as well as the aspect ratio of the connected pores significantly affect the elastic properties. We propose an inversion method to invert these three parameters simultaneously from experimental vertical P- and S-wave velocities using a global optimization algorithm. The method is applied to well log and seismic data from the Longmaxi shale reservoir in southwest China to verify its predictive ability.

1. Introduction

As extremely valuable unconventional resources, shale oil and gas have become a research focus for geophysical exploration and development. Compared to conventional reservoirs, shale reservoirs have more storage modes, greater mineral composition, more complex organics and pore types, and greater heterogeneity (Passey et al., 2010; Ma, 2016; Jiang et al., 2016). The establishment of an effective rock physics model for shale rocks is the basis for the study of geophysical response characteristics, which can provide a basis for the prediction of sweet spots in shale oil and gas reservoirs (Luo et al., 2020, 2021).

Unlike sandstones, shales are anisotropic, with vertical transverse isotropy (VTI), mainly due to the stratification of clay and kerogen (Hornby et al., 1994; Carcione, 2000; Lonardelli et al., 2007; Carcione and Avseth, 2015; Li et al., 2015; Zhang et al., 2017; Gong et al., 2021; Liu et al., 2022), horizontally distributed flat pores and microcracks (Hornby et al., 1994; Sarout and Guéguen, 2008; Dewhurst and Siggins, 2006; Baird et al., 2017), and long-term geological sedimentation and compaction processes (Lonardelli et al., 2007; Bandyopadhyay, 2009).

Rock physics experiments, which involve measuring properties such as resistivity, porosity, mechanical characteristics, and acoustic-electric properties, are essential tools for studying shale properties (Passey et al., 2010; Soeder, 1988; Gong et al., 2018, 2021). The experiments also play a crucial role in bridging well log responses and their interpretation (Luffel et al., 1992; Yang and Torres-Verdin, 2013). Sondergeld and Rai (2011) conducted experimental studies on the acoustic properties of Kimmeridge shale and found that shale anisotropy increases with the organic matter content. The rise in organic matter content leads to a decrease in density, which in turn produces effects opposite to those of compaction. Tan et al. (2015) using nuclear magnetic resonance (NMR) measurements of shale core plugs, investigated the NMR response characteristics of shale. Gong et al. (2019) obtained the static and dynamic properties of synthetic and natural shale samples containing various clay minerals through triaxial tests during loading and unloading processes.

Rock-physics models (Carcione et al., 2011; Grana et al., 2021; Yu et al., 2023; Guo et al., 2022a, 2022b), provide a basis for

---

* Corresponding author.
E-mail address: jba@hhu.edu.cn (J. Ba).
Peer review under the responsibility of China University of Petroleum (Beijing).

https://doi.org/10.1016/j.petsci.2025.06.021

describing elastic anisotropy. Many petrophysical models have been proposed. The differential effective medium (DEM) and self-consistent approximation (SCA) models are commonly used (e.g., Hornby et al., 1994; Qian et al., 2016; Gui et al., 2022; Zhu et al., 2024). Vernik and Landis (1996) and Carcione (2000) proposed the Backus average to describe the anisotropy caused by the lamination of clay and kerogen. Bandyopadhyay (2009) and Wu et al. (2012) considered kerogen as the background medium in the DEM theory. Pan et al. (2020) defined a brittleness indicator for high-porosity organic-rich shale reservoirs. Based on SCA and DEM methods. Qin et al. (2022) combined Backus averaging, DEM, and a linear slip model to describe the influence of inclined fractures in shale.

Compaction and diagenesis can change the orientation of mineral particles while compressing rock volumes (Lonardelli et al., 2007; Bandyopadhyay, 2009; Carcione and Avseth, 2015; Dabat et al., 2019). An orientation distribution function (ODF) and its standard deviation can be used for quantitative analysis (Sayer, 2005; Qian et al., 2016; Asaka et al., 2021; Gong et al., 2021; Huang et al., 2022). Hornby et al. (1994) proposed a technique to estimate the orientation distribution of clay platelets by using a digital scanning electron microscope, by which the effective elastic modulus of clay-fluid composites with different orientation angles can be estimated. The lamination degree is another indicator of mineral orientation and anisotropy (Guo et al., 2014). Zhang et al. (2017) proposed a workflow to describe anisotropy using the lamination degree and the aspect ratio of “clay-related” pores.

The pore connectivity of organic matter differs from that of clay minerals (Zhao et al., 2023; Yao et al., 2023). In general, connected and isolated pores coexist in shales. Fu et al. (2019) found a good correlation between the percentage of isolated pores and organic matter, indicating that isolated pores are primarily located in organic matter (Carcione, 2000). Dong et al. (2023) found that a large number of pores smaller than 100 nm in organic matter are disconnected. The effect of pore fluids is commonly analyzed with the Gassmann equation. The inclusion-based theory incorporates isolated pores (empty or fluid-saturated) as inclusions.

Seismic waves induce a fluid flow, and the differences in pore type and saturation can both affect the elastic properties (Kuteynikova et al., 2014; Chen et al., 2017; Ba et al., 2023). Therefore, a theory considering only one type of pore (isolated or connected) may lead to prediction errors, and modeling pore geometry accurately is essential (Wang et al., 2011; Li et al., 2016; Ma et al., 2019; Zhang et al., 2021). Wang and Tang (2021) proposed a method for predicting velocity dispersion from seismic data, based on a pore aspect ratio spectrum obtained with P-S velocity inversion (see also Li et al., 2013). Aspect ratio and pore orientation affect anisotropy (Falahat and Farrokhnia, 2020; Zidan et al., 2021; Guo et al., 2022b; Wu et al., 2023). Guo and Li (2015) estimated S-wave velocity by using the pore aspect ratio as a fitting parameter at each depth level and considering a statistical distribution of pore geometry, and Guo et al. (2022a) used the pore aspect ratio in AVO inversion. Global optimization algorithms such as simulated annealing (SA) (Kirkpatrick, 1984) and particle swarm optimization (PSO) (Kennedy and Eberhart, 1995) have been adopted. Gali and Waskito (2022) used PSO to estimate mineral stiffness and pore geometry, while Ba et al. (2023) used SA for the inversion of the wet-rock elastic modulus.

We propose a new theory, which combines the SCA-DEM model and Brown-Korringa equation. We first analyze the impact of isolated and connected pores on the elastic modulus and introduce a pore connectivity index (r_{con}). The theory takes into account the distribution of clay and kerogen by introducing a lamination index (LI). A sensitivity analysis, based on LI, r_{con}, and the isolated and connected pore aspect ratios, α_{iso}, and α_{con}, shows that LI, r_{con}, and α_{con} have a significant impact on stiffnesses and anisotropy. Therefore, these indicators are treated as unknown and inversion parameters, and the log P- and S-wave velocities are used as constraints in a SA inversion to obtain the depth variation of these parameters. This allows for a comprehensive consideration of the complexity of the pores and the degree of spatially varying particle orientation, bringing the model closer to real geological conditions. The main contribution of this work is the incorporation of the effects of clay lamination, pore types, and pore geometry into the rock physics modeling of shale rocks. Additionally, an inversion approach is employed to capture the depth-dependent variations of three key parameters—the lamination index, pore connectivity index, and connected pore aspect ratio—thereby enhancing the accuracy of the model predictions. The method is applied to log data from the Longmaxi shale in southwest China and compared with the other five approaches, demonstrating its effectiveness. The predicted elastic and anisotropy parameters are then applied to the seismic anisotropic VTI inversion, building the initial models.

2. Methodologies

2.1. Combined SCA-DEM model

Inclusion theory, based on SCA and DEM, is a typical approach used to estimate the elastic properties of rocks, where one component is usually regarded as the background medium, and the other as inclusions. SCA (Appendix A) is used to mix the fluid and solid phases, agreeing with the lower Hashin-Shtrikman limit as porosity exceeds 60% (Berryman, 1980; Fukuzawa et al., 1994). The rock is in a “grain suspension” unconnected state, in which the pore-fluid surrounds the solid phase, leaving the solid grains unconnected. Due to the symmetry of the SCA algorithm, both phases are only connected if porosity is between 40% and 60% (Qian et al., 2017). DEM (Appendix B), an asymmetric effective medium theory, assumes that one phase is initially the background medium, and the other is an inclusion (Norris, 1985; Zimmerman, 1984). Choosing different minerals as the background medium leads to different results, and thus to errors.

Hornby et al. (1994) proposed the anisotropic SCA-DEM model, where the volume fractions of both phases are set to 50%, and the SCA is used to build an interconnected effective medium. Then, the DEM model is applied to adjust the volume fraction of a phase to its actual value. It combines the advantages of both the SCA and DEM methods, and maintains the connectivity between different phases without defining a background medium, thus avoiding the limitations of the DEM.

Here, the SCA-DEM model is applied to obtain the properties of the clay-kerogen mixture. The physical and elastic properties of kerogen are more similar to those of fluids and are coupled with clay. When simulating a clay-kerogen mixture, it is unnecessary to consider the primary and secondary order of the two phases, while ensuring that both are interconnected.

2.2. Brown-Korringa model

Gassmann (1951) equations are

$$K_{\mathrm{sat}} = K_{\mathrm{dry}} + \left(1 - \frac{K_{\mathrm{dry}}}{K_{\mathrm{m}}}\right)^2 \left(\frac{\phi}{K_{\mathrm{fl}}} + \frac{1-\phi}{K_{\mathrm{m}}} - \frac{K_{\mathrm{dry}}}{K_{\mathrm{m}}^2}\right)^{-1}, \tag{1}$$

$$\frac{1}{\mu_{\mathrm{sat}}} = \frac{1}{\mu_{\mathrm{dry}}}, \tag{2}$$

where K_{sat} and μ_{sat} are the bulk and shear moduli of the saturated rock respectively, K_{dry} and μ_{dry} are those of the dry rock, K_{fl} and K

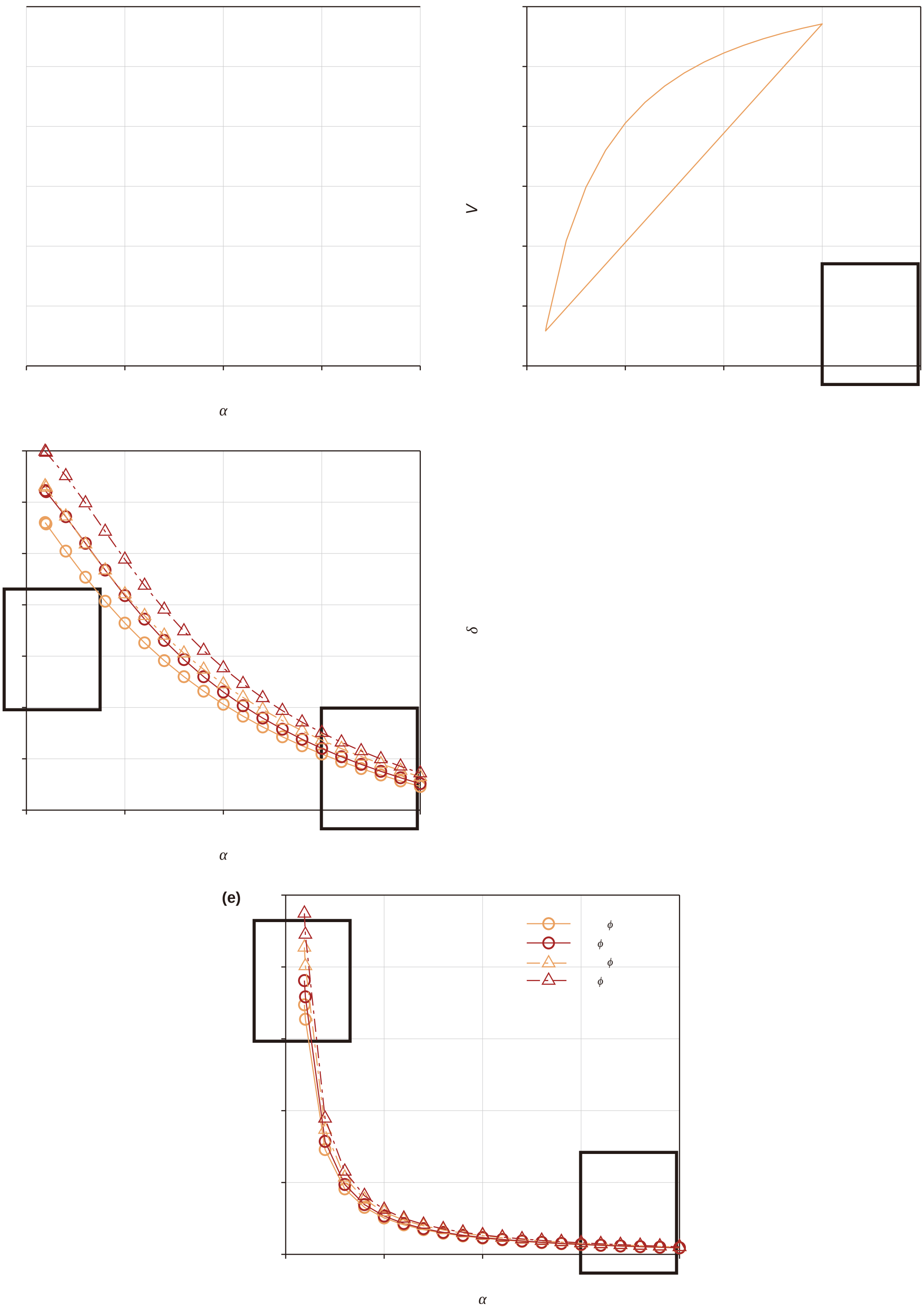

Fig. 1. **(a)** P- and **(b)** S-wave velocities and Thomsen parameters **(c)** ε, **(d)** δ, **(e)** γ as a function of pore aspect ratio (α) for porosities (ϕ) of 0.16 and 0.18 by using DEM (Model 1, orange) and BK (Model 2, red) models.

types should not be ignored and should be considered in shale modeling.

In this study, we employ the DEM model and the Brown-Korringa equation to quantify the differences in the elastic properties of shale with isolated and connected pores. However, besides pore connectivity, the differences between the two models can also be influenced by the elastic interactions of fluid-filled cracks (Zhao et al., 2020). As pores with small aspect ratios are

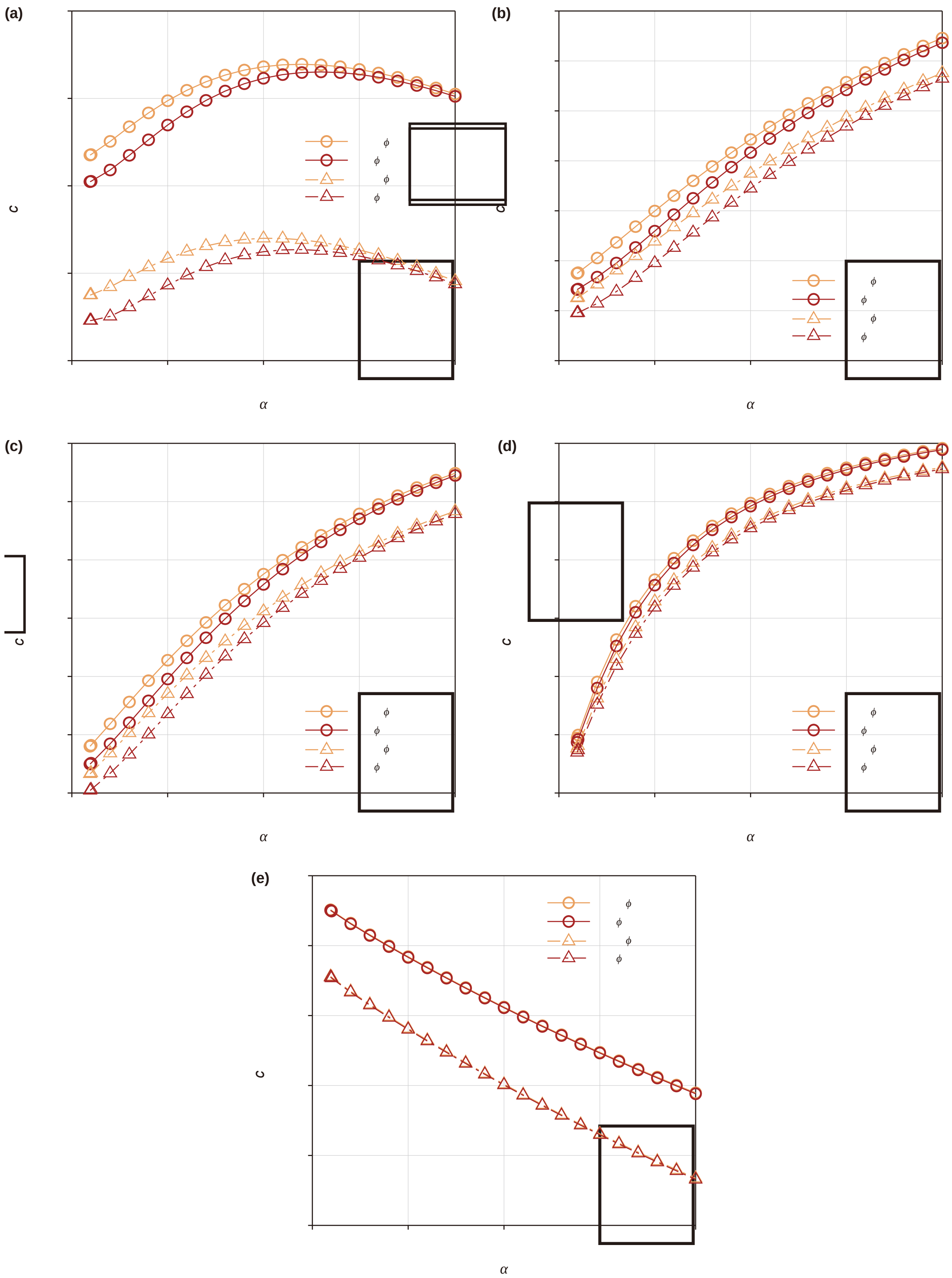

Fig. 2. **(a)** c_{11}, **(b)** c_{33}, **(c)** c_{13}, **(d)** c_{44}, and **(e)** c_{66} as a function of pore aspect ratio (α) for porosities (ϕ) of 0.16 and 0.18 by using the DEM (Model 1, orange) and BK (Model 2, red) models.

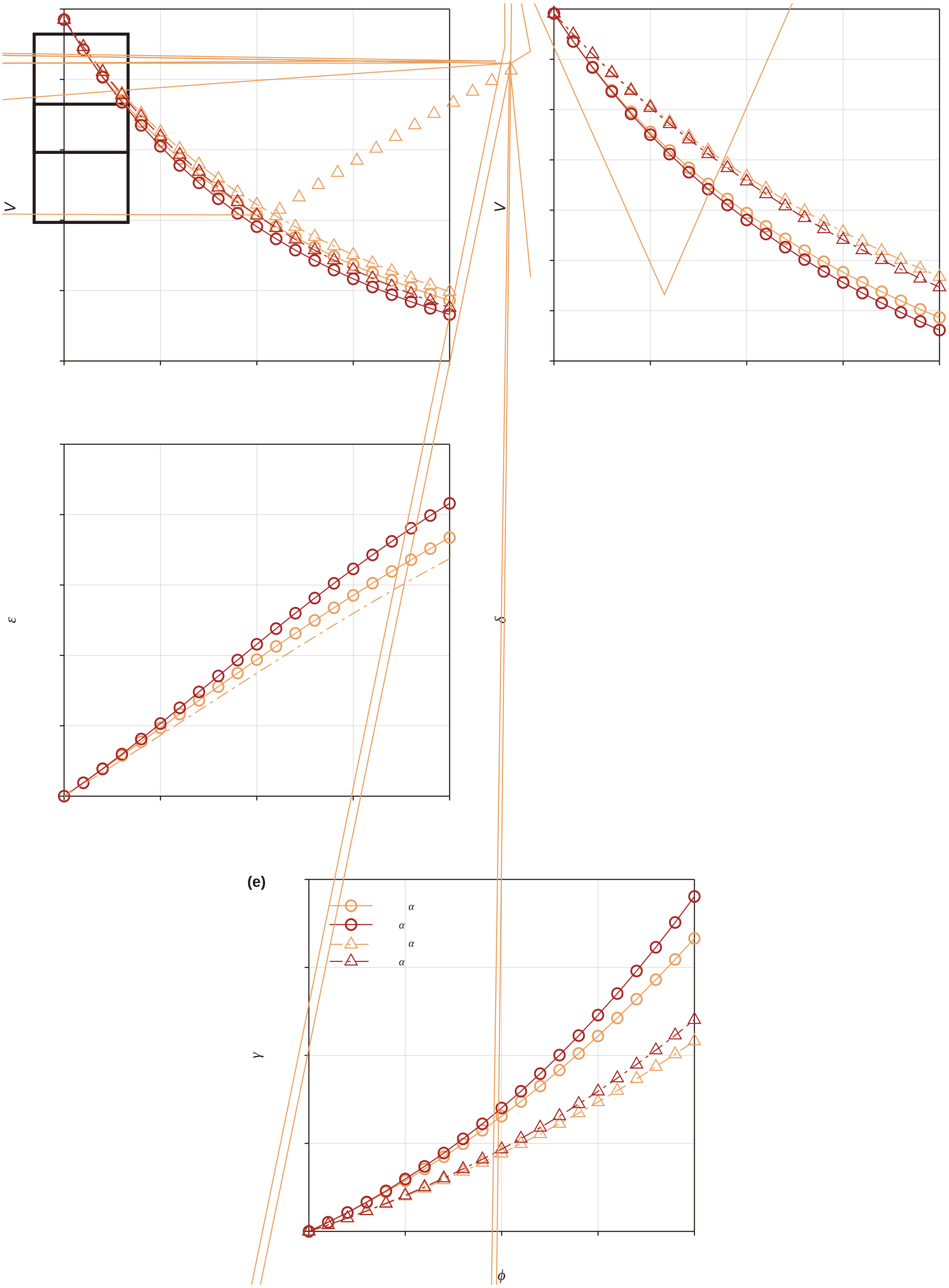

Fig. 3. **(a)** P- and **(b)** S-wave velocities and Thomsen parameters **(c)** ε, **(d)** δ, and **(e)** γ as a function of porosity (ϕ) for pore aspect ratios of (α) 0.05 and 0.07 by using DEM (Model 1, orange) and BK (Model 2, red) models.

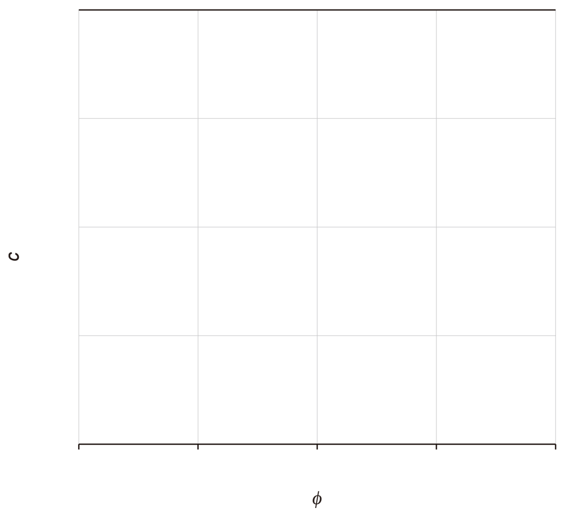

Fig. 4. **(a)** c_{11}, **(b)** c_{33}, **(c)** c_{13}, **(d)** c_{44}, and **(e)** c_{66} as a function of porosity (ϕ) for pore aspect ratios of (α) 0.05 and 0.07 by using the DEM (Model 1, orange) and BK (Model 2, red) models.

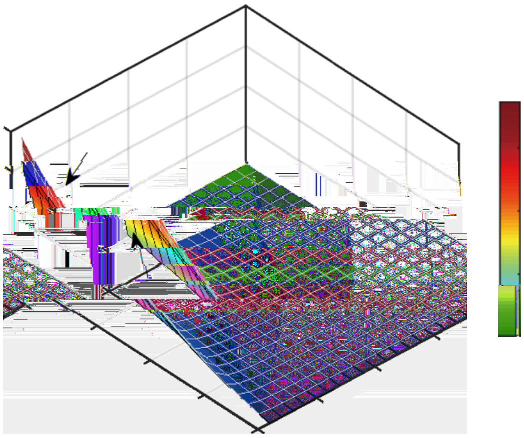

Fig. 5. Vertical **(a)** P- and **(b)** S-wave velocities and Thomsen parameters **(c)** , **(d)** δ, and **(e)** γ as a function of porosity (ϕ) and pore aspect ratio (α) by using the DEM (Model 1) and BK (Model 2) models, respectively.

closer to microcracks and experience stronger elastic interactions, this may amplify the discrepancies of the models, thereby affecting the quantification results of pore connectivity to some extent.

3.2. Effect of the pore indices

Based on the previous analysis, it is evident that pore type has a non-negligible influence on the elastic properties of shale. To describe the effect of the pore type (isolated or connected) quantitatively, we divided the porosity into two contributions, isolated and connected pore spaces, as

$$\phi = \phi_{\mathrm{con}} + \phi_{\mathrm{iso}}. \tag{8}$$

The connectivity and isolation indices are

$$r_{\mathrm{con}} = \phi_{\mathrm{con}}/\phi, \tag{9a}$$

$$r_{\mathrm{iso}} = \phi_{\mathrm{iso}}/\phi = 1 - r_{\mathrm{con}}, \tag{9b}$$

respectively, which express the relative fractions of connected pores and isolated pores.

The following analyzes the sensitivity of elastic parameters related to the volume proportions and aspect ratios of different pore types. The pore-related parameters analyzed here include the connectivity index r_{con}, the isolation index r_{iso}, the aspect ratios of the connected pores α_{con}, and the isolated pore α_{iso}. To demonstrate the necessity of introducing the pore connectivity index and to provide a basis for the selection of target parameters for subsequent inversion, we analyzed the variation of the stiffness coefficients and anisotropy parameters with respect to the two sets of parameters [r_{iso}, α_{iso}]/[r_{con}, α_{con}]. A simplified shale model was used for numerical analysis, with the effective elastic moduli of brittle minerals set to $K_{\mathrm{brittle}} = 78.66$ GPa and $\mu_{\mathrm{brittle}} = 53.8$ GPa, and the other parameters are the same as Section 3.1. The parameter variations were examined when the values of r_{iso} and r_{con} were 0.01, 0.25, 0.5, 0.75, and 1, respectively.

Fig. 6 illustrates the variations in stiffness coefficient group {c_{11}, c_{33}, c_{13}, c_{44}, c_{66}} at different isolated pore proportions (r_{iso}) simulated by the shale model, as the isolated pore aspect ratio (α_{iso})

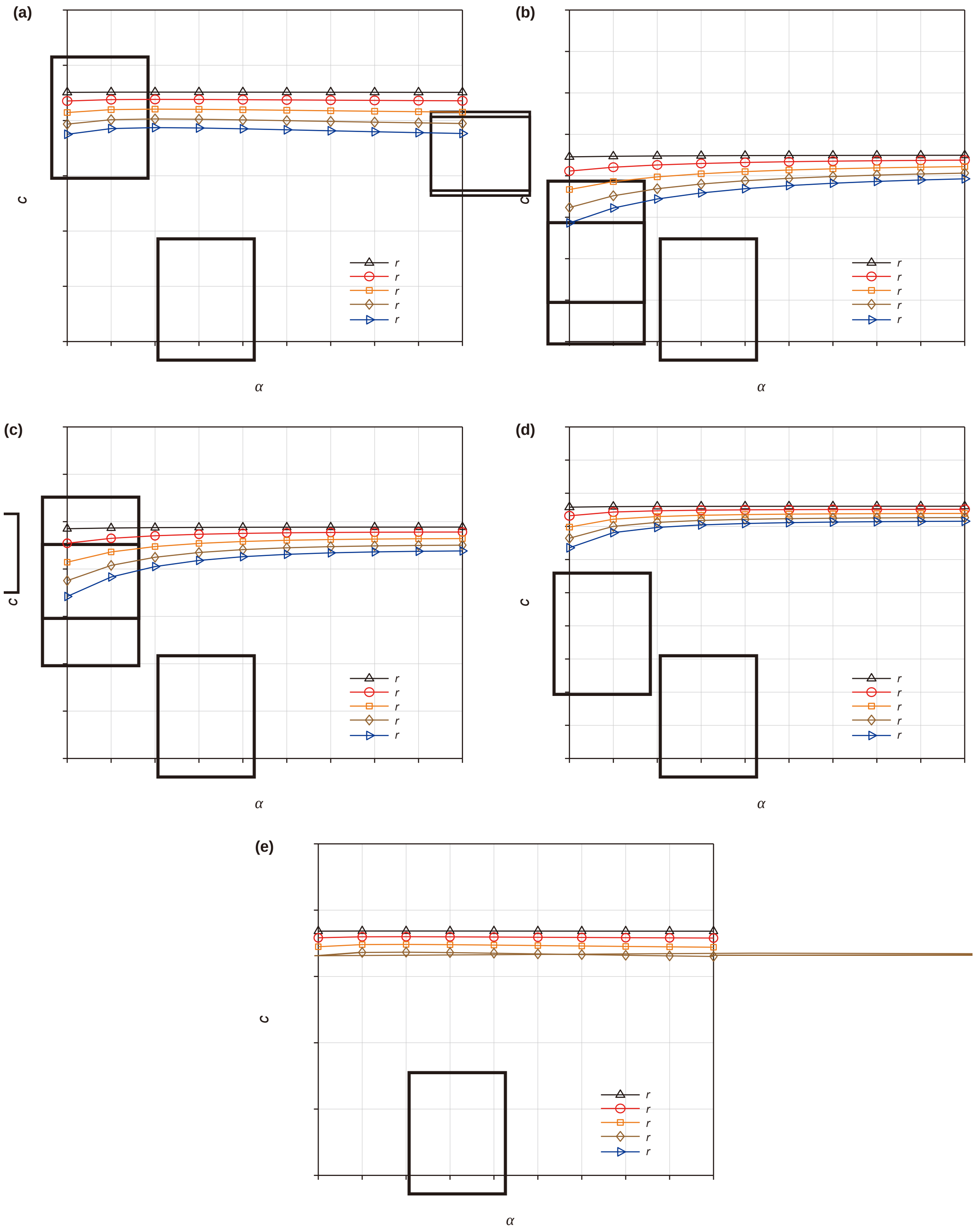

Fig. 6. **(a)** c_{11}, **(b)** c_{33}, **(c)** c_{13}, **(d)** c_{44}, and **(e)** c_{66} as a function of α_{iso} with different r_{iso}.

changes. Fig. 6(a), (d) show that c_{11} and c_{66} change little with α_{iso} under different isolation index r_{iso}. Fig. 6(b), (c) indicate that c_{33} and c_{44} only exhibit a slow variation with isolated pore aspect ratio α_{iso} when r_{iso} is high. Fig. 7 shows the variation in the stiffness coefficients with the connected pore aspect ratio (α_{con}) under different connectivity indices (r_{con}). As α_{con} increases, both c_{11} and c_{66} gradually decrease, while c_{13}, c_{33}, and c_{44} increase. All five stiffness coefficients decrease as the r_{con} increases.

Comparing Fig. 7 with Fig. 6, it is observed that the connected pore aspect ratio (α_{con}) and connectivity index (r_{con}) result in greater changes in the stiffness coefficients compared to that of the isolated pores (α_{iso} and r_{iso}), indicating that shale elastic parameters are more sensitive to the parameters related to the connected pores (α_{con} and r_{con}).

Fig. 8 shows the anisotropic parameter group $\{V_{\text{P}}, V_{\text{S}}, \ \delta, \gamma\}$ changing with the isolated pore aspect ratio (α_{iso}) and the

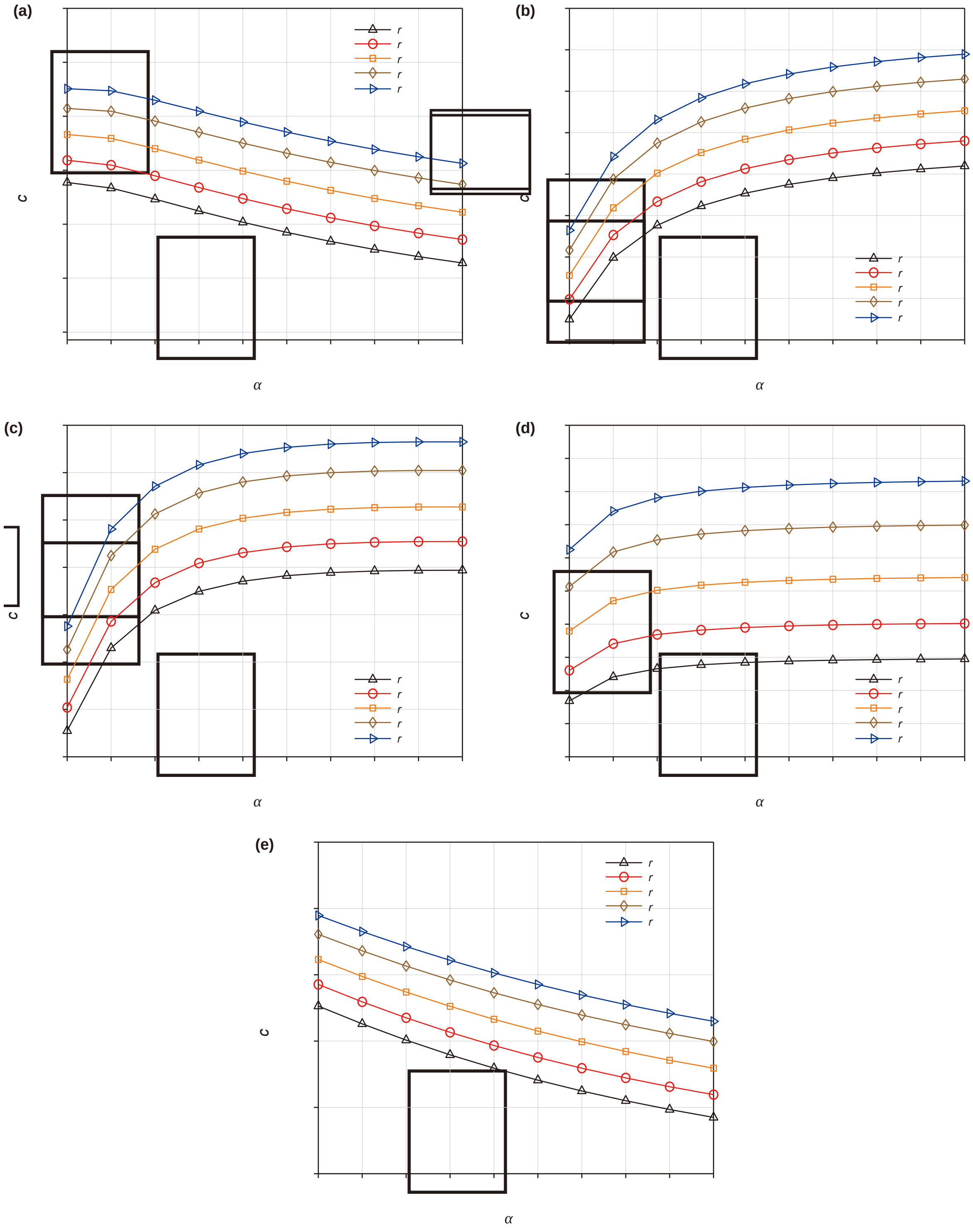

Fig. 7. **(a)** c_{11}, **(b)** c_{33}, **(c)** c_{13}, **(d)** c_{44}, and **(e)** c_{66} as a function of α_{con} for different r_{con}.

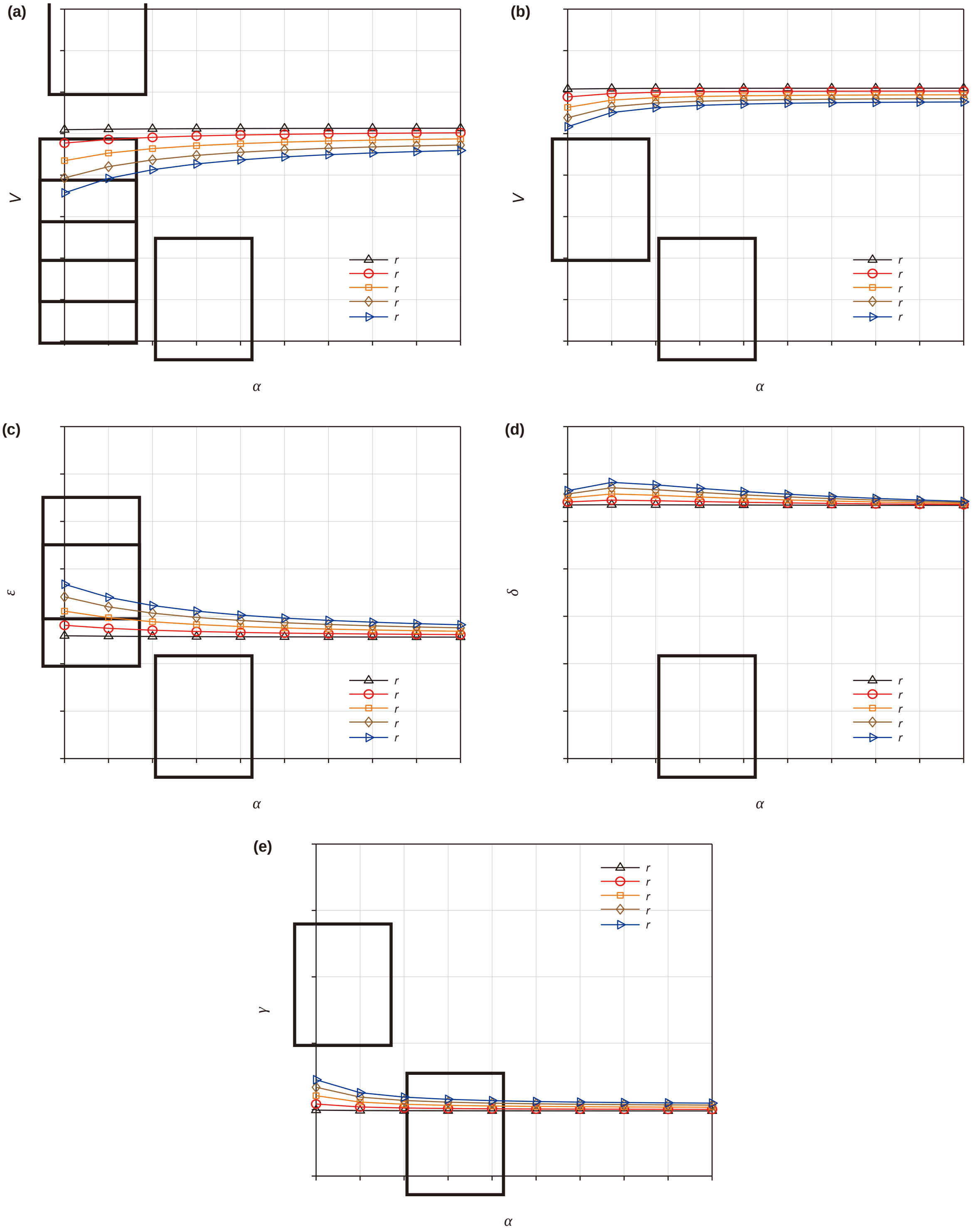

Fig. 8. (**a**) P- and (**b**) S-wave velocities and Thomsen parameters (**c**) , (**d**) δ, and (**e**) γ as a function of α_{iso} with different r_{iso}.

isolation index (r_{iso}). It can be seen that as r_{iso} increases, V_{P} and V_{S} decrease, while the other three parameters increase, though the overall numerical range remains small. The anisotropic parameters only exhibit noticeable changes when the α_{iso} is small, and as α_{iso} increases, the changes induced by r_{iso} become smaller. Fig. 9 shows the changes in the group {V_{P}, V_{S}, , δ, γ} with α_{con} and r_{con}. It can be observed that as α_{con} increases, both V_{P} and V_{S} increase, while , δ, and γ show a significant downward trend. Additionally, with larger r_{con} values, V_{P}, V_{S}, and δ decrease, whereas and γ increase.

By comparing Figs. 8 and 9, it can be observed that the connected pore aspect ratio (α_{con}) and connectivity index (r_{con}) have a more significant impact on P-/S-wave velocities, as well as anisotropic parameters. This indicates that connected-pore-related parameters α_{con} and r_{con} are more sensitive to the changes in elastic parameters.

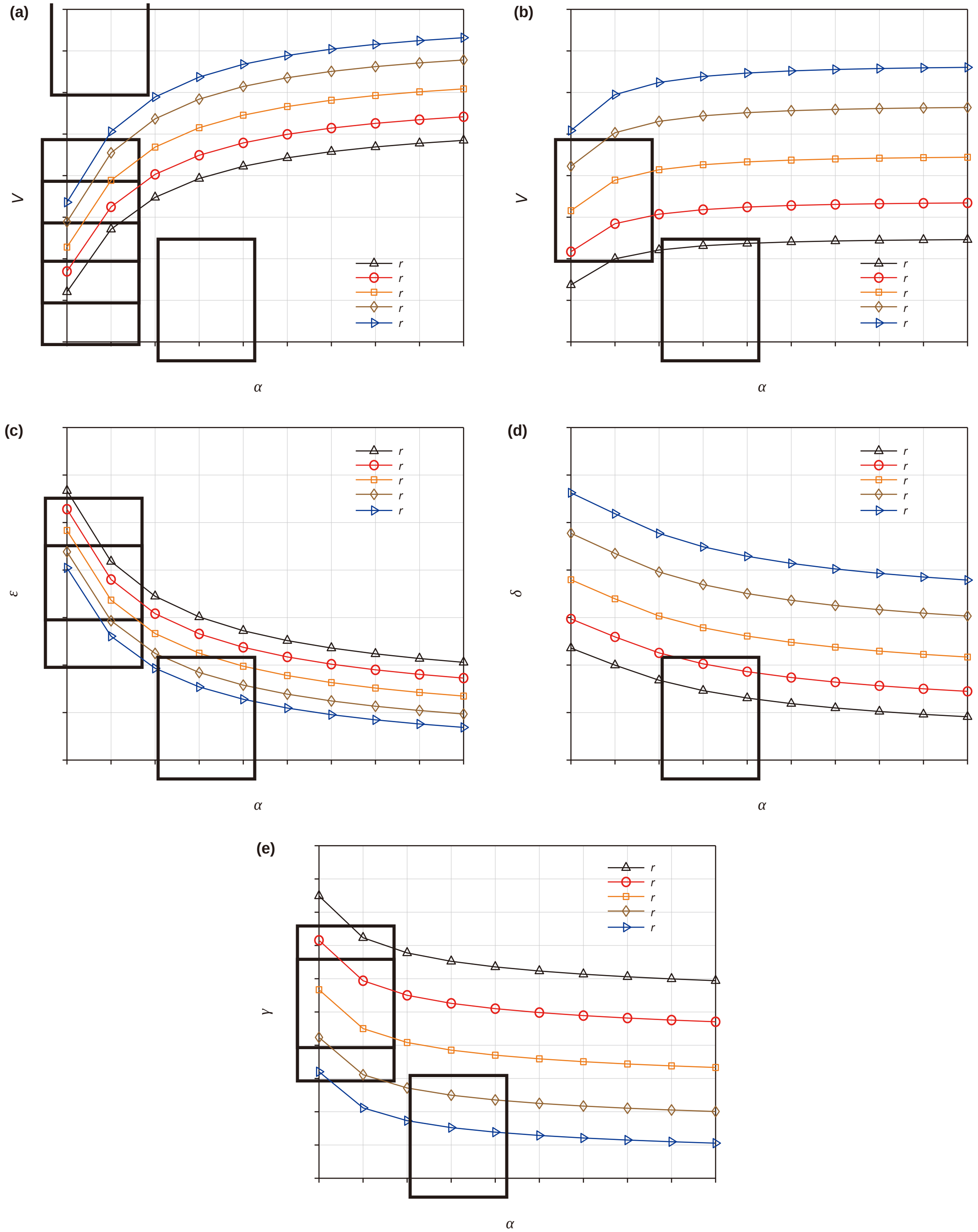

Fig. 9. (**a**) P- and (**b**) S-wave velocities and Thomsen parameters (**c**) , (**d**) δ, and (**e**) γ as a function of α_{con} with different r_{con}.

3.3. *Effects of the preferred orientation of the clay and kerogen layers*

Clay-kerogen layers often exhibit a preferred orientation and induce anisotropy (Vernik and Nur, 1992; Hornby et al., 1994; Carcione, 2000). Qian et al. (2016, 2017) assumed that the deflection angle of clay-kerogen layers platelets follows a normal distribution. The standard deviation of the distribution controls the strength of the lamination.

We define a rotation angle (θ) of each platelet, i.e., the angle between the symmetry axis of the normally distributed clay-kerogen platelets and the vertical direction. The elastic properties of platelets at different rotation angles can be derived from the Bond transformation of the horizontal ones (Mavko et al., 2009). The orientation distribution function (ODF) is

$$\text{ODF} \sim \text{N}(mean, \text{LI}), \tag{10}$$

where "*mean*" represents the average value of the rotation angle. Since the main lamination direction of the stratum is horizontal, the parameter "*mean*" is usually set to zero. "LI" refers to the standard deviation of the normal distribution, which indicates the degree of disorder of the platelets. The probability density function of the preferred orientation is

$$\nu(\theta, \mathrm{LI}) = \frac{1}{\sqrt{2\pi}} \exp\left(-\frac{\theta^2}{2\mathrm{LI}^2}\right). \tag{11}$$

The Voigt-Reuss-Hill (VRH) average is used to estimate the effective elastic stiffness (Voigt) and compliance (Reuss) matrices of the layers composed of rotated clay-kerogen platelets (Hornby et al., 1994), as

$$\mathbf{C}_{\mathrm{mix}} = \frac{1}{2\pi} \int_0^{2\pi} \int_{-\pi/2}^{\pi/2} \nu(\theta, \mathrm{LI})\, \mathbf{C}_{\mathrm{rot}}(\theta, \phi)\, \mathrm{d}\theta\, \mathrm{d}\phi, \tag{12}$$

$$\mathbf{S}_{\mathrm{mix}} = \frac{1}{2\pi} \int_0^{2\pi} \int_{-\pi/2}^{\pi/2} \nu(\theta, \mathrm{LI})\, \mathbf{S}_{\mathrm{rot}}(\theta, \phi)\, \mathrm{d}\theta\, \mathrm{d}\phi, \tag{13}$$

respectively, where φ is the azimuth angle, $\mathbf{C}_{\mathrm{rot}}(\theta, \phi)$ and $\mathbf{S}_{\mathrm{rot}}(\theta, \phi)$ refer to the stiffness and compliance matrices of the platelets after the Bond transformation, respectively. Then, the VRH average is

$$\mathbf{C}_{\mathrm{clay}} = \left[\mathbf{C}_{\mathrm{mix}} + (\mathbf{S}_{\mathrm{mix}})^{-1}\right] \Big/ 2. \tag{14}$$

and the effective modulus of the clay-kerogen platelets rotated at specific angles is computed by the Bond transformation:

$$\mathbf{C}_{\mathrm{rot}}(\theta, 0) = \mathbf{L}_{\mathrm{im}} \mathbf{L}_{\mathrm{jn}} \mathbf{L}_{\mathrm{kp}} \mathbf{L}_{\mathrm{lp}} \mathbf{C}_{\mathrm{ck}}(0, 0), \tag{15a}$$

$$\mathbf{L}_{\mathrm{ij}} = \begin{bmatrix} 1 & 0 & 0 \\ 0 & \cos\theta & -\sin\theta \\ 0 & \sin\theta & \cos\theta \end{bmatrix}, \tag{15b}$$

where the platelets are rotated by angle φ around the vertical symmetry axis.

$$\mathbf{C}_{\mathrm{rot}}(\theta, \varphi) = \mathbf{L}_{\mathrm{im}} \mathbf{L}_{\mathrm{jn}} \mathbf{L}_{\mathrm{kp}} \mathbf{L}_{\mathrm{lp}} \mathbf{C}_{\mathrm{ck}}(\theta, 0), \tag{16a}$$

$$\mathbf{L}_{\mathrm{ij}} = \begin{bmatrix} \cos\varphi & -\sin\varphi & 0 \\ \sin\varphi & \cos\varphi & 0 \\ 0 & 0 & 1 \end{bmatrix}; \tag{16b}$$

φ ranges from 0 to 2π with an interval of π/3, and $\mathbf{C}_{\mathrm{ck}}$ is the stiffness matrix of the clay-kerogen mixture.

In shale modeling, the rotation angle of the clay-kerogen platelets follows a normal distribution to simulate clay lamination. The lamination index LI, the standard deviation of the rotation angles, quantifies the degree of lamination, while the expectation (*mean*), as the average value of the angles, represents the overall lamination direction of the clay layers. To examine the effects of LI on the anisotropy, we plot (c_{11}, c_{33}, c_{13}, c_{44}, c_{66}) and (V_{P}, V_{S}, δ, γ) as a function of LI for different *mean* values. As shown in Figs. 10 and 11, all the parameters show the most significant variations at low LI and gradually stabilize as LI increases. When expectations differ, although the initial values and trends of the elastic parameters are different, they ultimately converge to a stable value, indicating that the anisotropy of shale weakens as LI increases. It is because as LI increases, the clay-kerogen platelets tend to form a more random and disordered arrangement, reducing the overall lamination and VTI properties of shale rocks. The numerical analysis above highlights the noticeable LI-induced changes in the elastic parameters, indicating that LI exhibits a strong sensitivity to the elastic properties.

3.4. The modeling-inversion approach

Based on numerical analyses above, we emphasize the importance of considering the clay-kerogen lamination, pore types, and pore aspect ratios in shale modeling. The parameter r_{con} is introduced to control the proportion of isolated and connected pores, adjusting their respective impacts. The aspect ratios (α_{con} and α_{iso}) refine the pore morphology, while the lamination index (LI) governs the clay-kerogen mixture, managing the intrinsic anisotropy of shale rocks. By incorporating depth-dependent variations of r_{con}, α_{con}, and LI, the shale model can be calibrated for improved simulation accuracy to some extent. As discussed in Section 3.2, α_{con} has a significant impact on elastic properties, whereas α_{iso} plays a minor role. To mitigate the ill-posedness of the inverse problem, we limit the number of the inverted parameters. Thus, LI, r_{con}, and α_{con} are selected as the target parameters, while α_{iso} is held constant based on the preliminary test. We propose a new shale modeling strategy that accounts for the spatial variations of these three auxiliary parameters. An inversion strategy, utilizing a global optimization algorithm, is employed to minimize the objective function and obtain the optimal solutions. The inversion results of these parameters refine the shale model, bringing it closer to actual geological conditions.

As mentioned above, crack-like pores within clay contribute significantly to shale anisotropy (Hornby et al., 1994; Kwon et al., 2004; Sarout and Guéguen, 2008; Zhang et al., 2017). Researches by Fu et al. (2019) and Dong et al. (2023) indicate that isolated pores/cracks primarily develop in the organic matter of shale rocks. Consequently, in this modeling, we assume the presence of isolated pores/cracks in the clay-kerogen mixture and incorporate them accordingly. Additionally, Yao et al. (2023) highlighted that the connectivity between organic pores and inorganic pores plays a crucial role in hydrocarbon migration. While the literature does not explicitly indicate that connected pores are exclusively developed in either organic matter or inorganic materials, we have included connected pores in both the clay-kerogen mixture and the brittle minerals in our model.

The workflow is as follows:

(1) The properties of the clay-kerogen mixture are obtained by using the SCA-DEM method, as explained in Section 2.1.
(2) Isolated pores/cracks mainly develop in organic matter (Fu et al., 2019; Dong et al., 2023). An anisotropic DEM model is utilized to add isolated flat microcracks with a porosity of ϕ_{iso} into the clay-kerogen mixture, resulting in clay-kerogen platelets.
(3) Based on the orientation distribution function (ODF) and combined with the Bond transformation and VRH average, the clay-kerogen platelets are rotated and stacked according to a normal distribution to obtain the corresponding elastic properties. The lamination index is introduced to quantify the orientation of the platelets.
(4) Minerals are mixed by using the VRH average to obtain the effective modulus of the effective mineral. Then this mixture is added to the medium of step (3) using the anisotropic DEM model to obtain the properties of the skeleton.
(5) The modeling assumes that connected pores develop in the clay-kerogen mixture as well as in the effective mineral (Yao et al., 2023). Using the anisotropic DEM model,

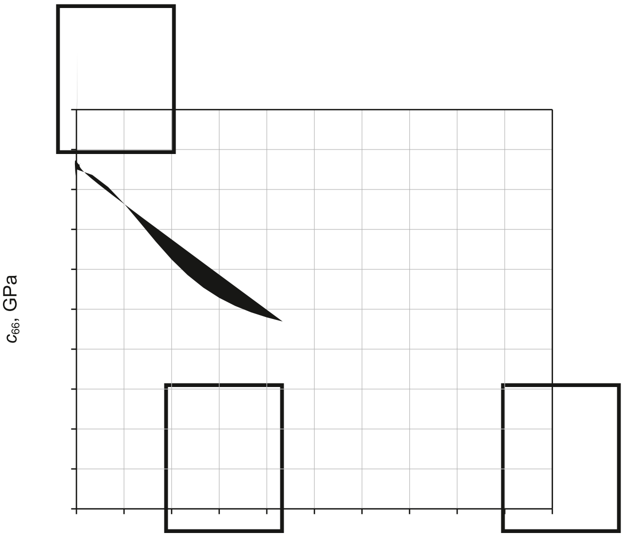

Fig. 10. **(a)** c_{11}, **(b)** c_{33}, **(c)** c_{13}, **(d)** c_{44}, and **(e)** c_{66} as a function of the lamination index (LI) with different *mean* values.

connected dry pores with a porosity ϕ_{con} are added into the medium obtained in step (4), giving the properties of the dry shale.

(6) Based on the BK model, fluid (or a fluid mixture) is substituted into the pores of the dry medium to obtain the stiffnesses of the fluid-saturated shale.

(7) The residuals between the predicted and experimental (log) P- and S-wave velocities are minimized. The above three parameters are iteratively inverted. With the P-wave (V_{P}) and S-wave (V_{S}) velocities as constraints, the inversion objective function is

$$\widehat{\mathbf{m}} = \underset{\mathbf{m}}{\text{argmin}}\left[\sigma_1\left\|V_{\text{P}}^{\text{pred}}(\mathbf{m}) - V_{\text{P}}^{\text{real}}\right\|_2 + \sigma_2\left\|V_{\text{S}}^{\text{pred}}(\mathbf{m}) - V_{\text{S}}^{\text{real}}\right\|_2\right], \tag{17}$$

where $\mathbf{m} = [\alpha_{\text{con}}, r_{\text{con}}, \text{LI}]$, σ_1 and σ_2 are scaling parameters for balancing the misfit, while V^{pred} and V^{real} denote the theoretical and experimental velocities, respectively. Considering that V_{S} is

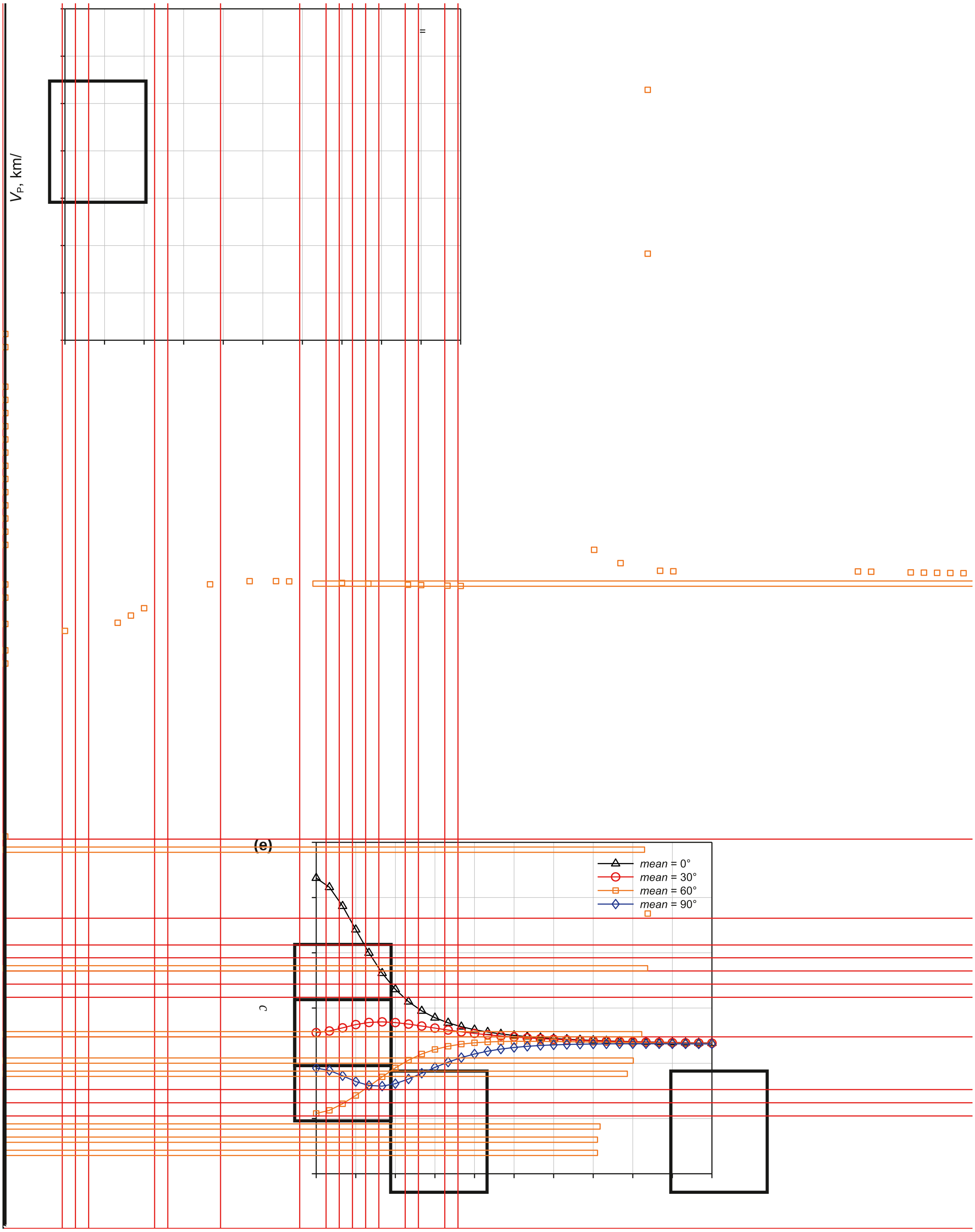

Fig. 11. (**a**) P- and (**b**) S-wave velocities and anisotropy parameters (**c**) , (**d**) δ, and (**e**) γ as a function of the lamination index (LI) for different *mean* values.

smaller than V_P, we set σ_2 greater than σ_1. Due to the high nonlinearity, the SA algorithm is adopted to solve this inverse problem.

(8) The inverted parameters from step (7) are used in the shale model to obtain the final properties.

Fig. 12 illustrates the workflow from steps 1 to 6, while Fig. 13 shows the workflow for the shale model aided by the inversion strategy.

The physical and elastic properties of kerogen are more similar to those of fluids, which are quite different from other brittle minerals. Kerogen is commonly coupled with clay. Therefore,

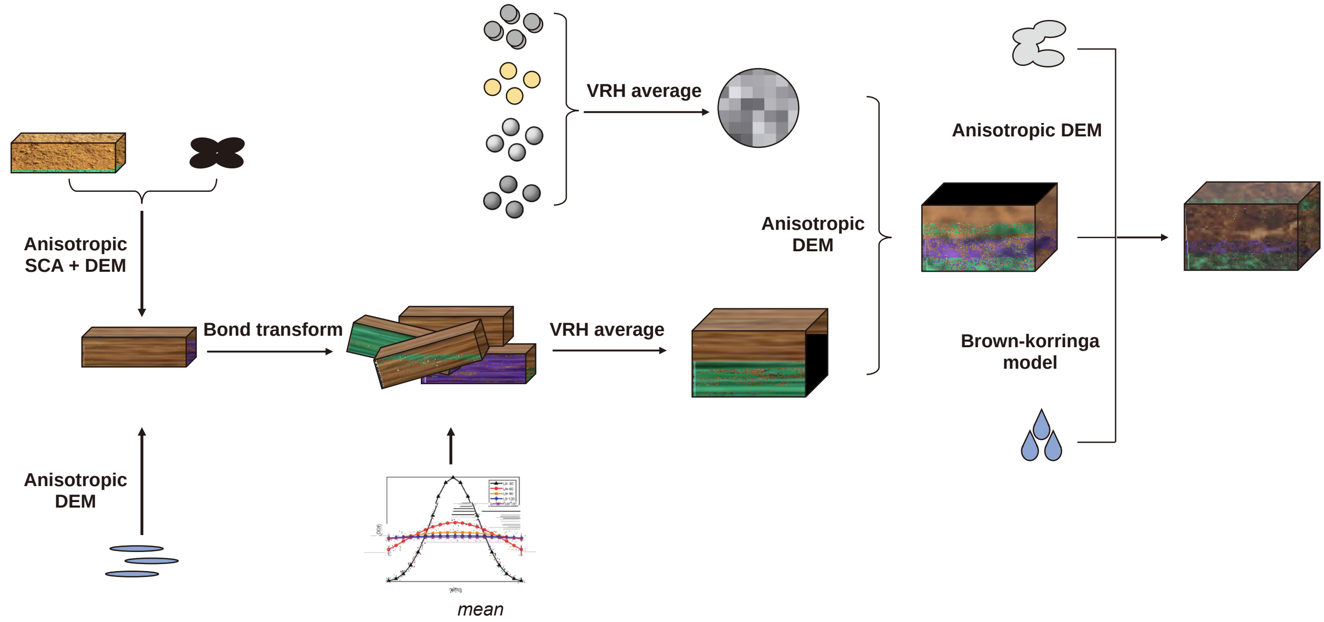

Fig. 12. Shale modeling scheme considering clay-kerogen lamination and isolated and connected pores.

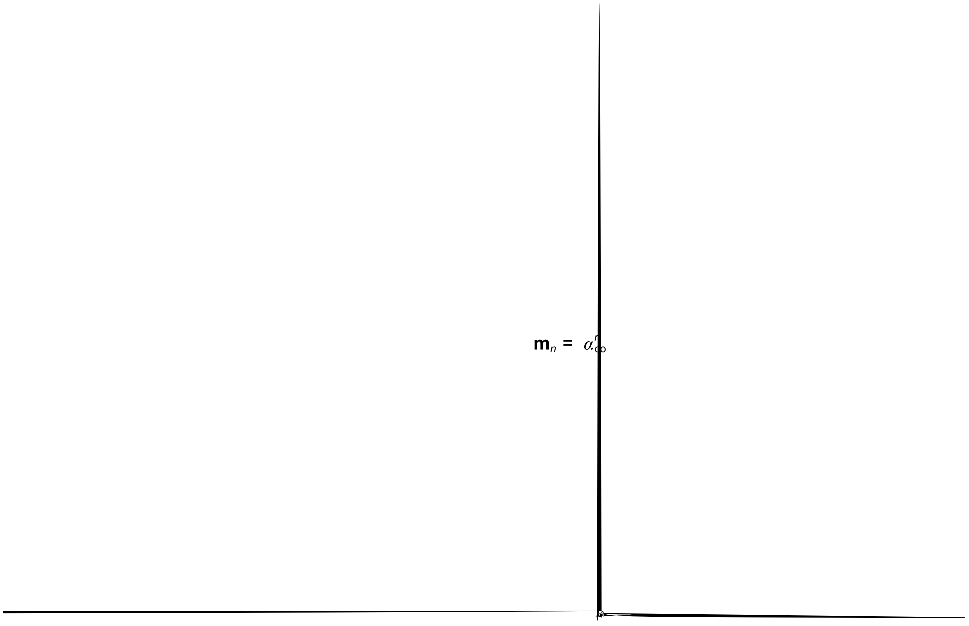

Fig. 13. Workflow of the inversion-aided modeling.

when calculating the equivalent elastic properties of the clay-kerogen mixture, the interconnection between the two components must be taken into account (Qian et al., 2016). The SCA model can achieve this interconnection between the two-phase materials. However, the volume fractions of clay and kerogen vary with depth, it is difficult to choose either clay or kerogen as the background phase. Moreover, the kerogen concentration may fall outside the biconnected range of SCA (40%–60%). To address these issues, we use SCA-DEM to model the clay-kerogen mixture. The SCA-DEM does not need to consider the order in which the two-phase materials are added, ensuring their interconnection and effectively combining the advantages of both theories (Hornby et al., 1994; Berryman, 1980; Mavko et al., 2009; Qian et al., 2016).

The DEM model, under the high-frequency assumption, can simulate the distribution of inclusions within the background phase. When incorporating brittle minerals and pores, the background phase and the order of addition have already been determined, enabling the use of DEM to include the brittle minerals and pores. The isotropic brittle minerals in shale are typically discretely distributed in the clay-kerogen background phase (Wu et al., 2012; Qian et al., 2016). Therefore, DEM method can be employed to add brittle minerals into the background phase (Bandyopadhyay, 2009; Zhang et al., 2017).

4. Example

4.1. Preliminary test

We used log data from the Longmaxi shale reservoir in Southwest China for testing the proposed method. At the well location, the shale reservoir is located between 2051 m and 2063 m in depth. Fig. 14 displays the log profiles, showing data of Well 1 for the P-wave velocity (V_P), S-wave velocity (V_S), density (ρ), porosity (ϕ), and the mineral components (fraction). The rocks in the reservoir formation include brittle minerals, e.g. quartz, calcite, and dolomite, and a relatively high volume of clay and organic content. Due to the reservoir section belonging to the ancient Upper Ordovician, the shale rocks have been highly compacted, resulting in porosities of less than 5%. Additionally, the shale has a high maturity, with the vitrinite reflectance ranging from 2 to 2.5. Fig. 15 presents photomicrographs of the shale samples from the study area. In these images, we can observe flat isolated pores within the organic matrix (Fig. 14(a)), which are typically discrete. In contrast, the inter-particle pores and cracks (Fig. 14(b)) are generally interconnected. In the subsequent analysis, we apply the proposed method to account for both isolated and connected pores, as well as the lamination of clay-kerogen mixtures.

Fig. 14. The logging data of Well 1 including P- and S-wave velocities, density, porosity, and mineral fractions.

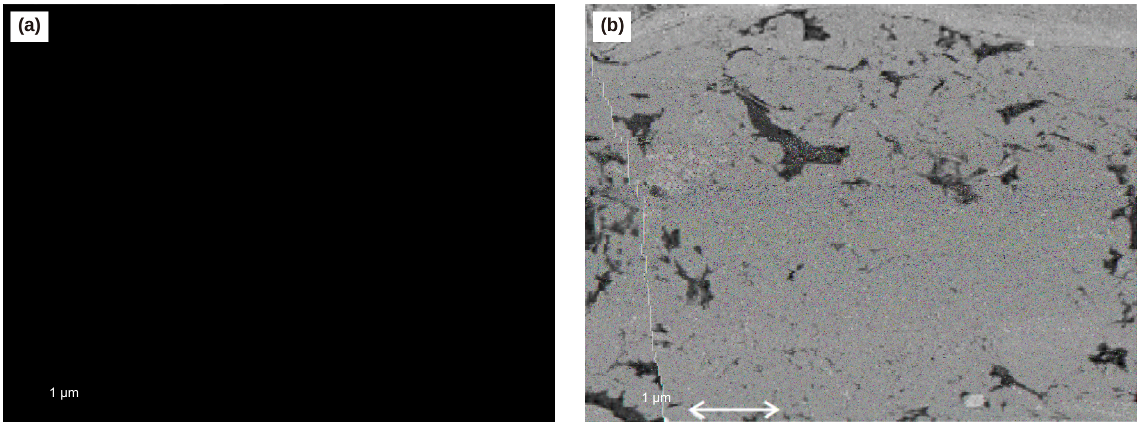

Fig. 15. The photomicrograph of the shale samples from the study area, showing **(a)** flat isolated pores within the organic matter and **(b)** connected interparticle/dissolution pores.

The volume fractions of Kerogen and clay, porosity, etc. can be obtained from the log data, while the stiffness moduli can be determined through the literature (see Table 2). The unknown parameters are limited to the pore-related ones (aspect ratios and proportions of different pore types), and the lamination-related ones (expectation *mean* and standard deviation LI of the rotation angles of the clay-kerogen platelets). To ensure that the medium exhibits VTI properties, the expectation *mean* of the normal distribution is set to 0° (Qian et al., 2016). We conducted a preliminary inversion test to determine a reasonable aspect ratio of the isolated pores. Specifically, we set other parameters to constant values and focused on inverting α_{iso} only by minimizing the residuals between the predicted and the experimental P- and S-wave velocities. The results are shown in Fig. 16, where the variation in the aspect ratio of the isolated pores (α_{iso}) is quite small, ranging from 0.01 to 0.05. Furthermore, the estimated results for most layers are mainly around 0.01. This indicates that the aspect ratio of the isolated pores hardly contributes to the anisotropy and elastic properties of the shale, which is consistent with the preceding sensitivity analysis. Therefore, we assumed it a constant value of 0.01. Furthermore, the results of this inversion test also indicate that the isolated pores in this study area are mainly flat microcracks (corresponding to small aspect ratios).

4.2. *Tests for the inversion-aided modeling*

After determining α_{iso}, we invert the three unknown parameters, namely, LI, r_{con}, and α_{con}. To verify the effectiveness of the proposed inversion-aided modeling method and the influence of the three auxiliary parameters, we propose six modeling tests. Each set examines the effects of different parameters.

1. Test 1: set LI, r_{con}, and α_{con} constant;
2. Test 2: invert LI with r_{con} and α_{con} constant;
3. Test 3: invert α_{con} with LI and r_{con} constant;
4. Test 4: invert r_{con} with LI and α_{con} constant;
5. Test 5: invert r_{con} and α_{con} with LI constant;
6. Test 6: invert LI, r_{con}, and α_{con}.

Table 2
Properties for the minerals and fluid (Mavko et al., 2009).

	Bulk modulus, GPa	Shear modulus, GPa	Density, g/cm^3
Quartz	37	44	2.65
Calcite	77	32	2.71
Dolomite	95	45	2.87
Clay	25	9	2.55
Kerogen	2.9	2.7	1.30
Brine	2.2	0	1.04

In each set of tests, the inverted parameters were then used to modify the established rock physics model, which in turn was adopted to predict the elastic and anisotropic parameters of the shales. The main purpose was to analyze the impact of different parameters on the model modification and prediction results. In all test cases, except for the parameters to be tested, all other values (including moduli) are set as fixed and remain consistent across each test case. This is designed to assess the model's prediction results under varying parameter conditions and to ensure the reliability of the test results.

Test 1: We set LI $= 1$, $r_{con} = 0.9$, and $\alpha_{con} = 0.8$. The theoretical P- and S-wave velocities, density, and anisotropic parameters are shown in Fig. 17. To quantify the differences, we calculated the relative root mean square errors (RRMSE) and correlation coefficients (CC) between the theoretical and experimental P- and S-wave velocities, as shown in Table 3. The results exhibit significant errors.

Test 2: This test considers the effect of LI varying with depth with $r_{con} = 0.9$, and $\alpha_{con} = 0.8$. The results are shown in Fig. 18. The errors are indicated in Table 3. Within the target layer, between 2.055 and 2.058 km, LI shows a significant variation, indicating that the clay lamination is relatively weak, indicating quasi-isotropy. Compared to Test 1, the errors of Test 2 are noticeably lower, demonstrating that considering the effects of the lamination index LI improves the prediction accuracy.

Test 3: This test considers the effect of α_{con} varying with depth, with LI $= 1$ and $r_{con} = 0.6$. The results are shown in Fig. 19, where the red curve represents the inverted α_{con}. The results for P- and S-wave velocities show an improvement compared to Tests 1 and 2. The errors are shown in Table 3.

Test 4: In this test, the effect of r_{con} varying with depth is considered, with LI $= 1$ and $\alpha_{con} = 0.3$ (Fig. 20). The errors are shown in Table 3. Compared to the previous three tests, the accuracy of the S-wave velocity has improved.

Test 5: This test inverts for α_{con} and r_{con} with LI $= 1$. Fig. 21 displays the results, with the red curves showing α_{con} and r_{con}. The test reveals significantly smaller errors for both velocities, with the RMSEs of the P- and S-wave velocities decreasing and the CCs improving (see Table 3).

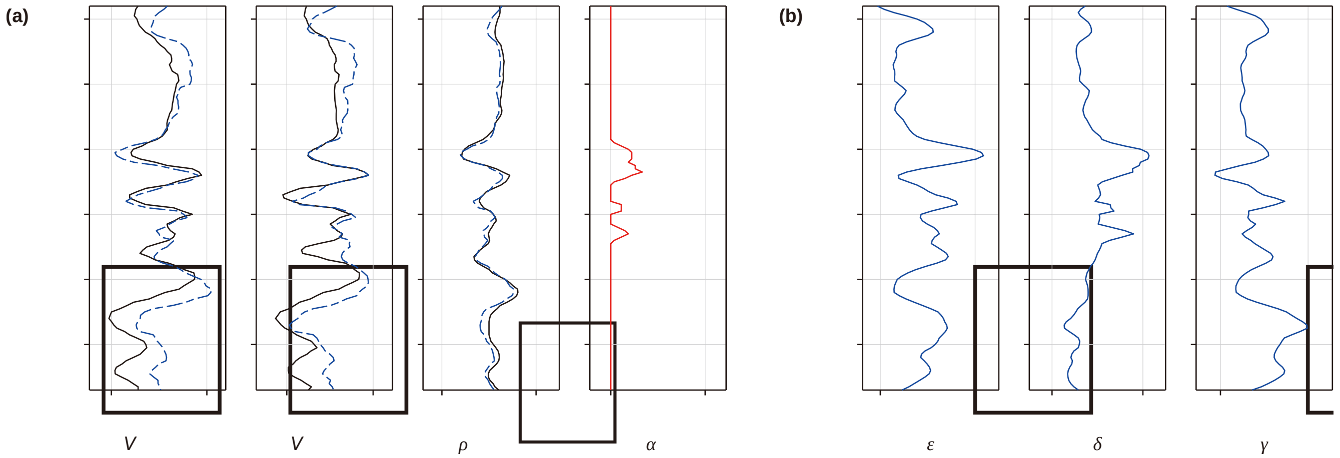

Fig. 16. **(a)** Comparison of experimental (black solid) and theoretical (blue dashed) P- and S-wave velocities and density of Well 1 by the modeling workflow in Fig. 12, based on the inverted isolated pore aspect ratio α_{iso} (red solid) for LI $= 1$, $r_{con} = 0.6$, and $\alpha_{con} = 0.3$. **(b)** Anisotropic parameters ε, δ, and γ (blue solid).

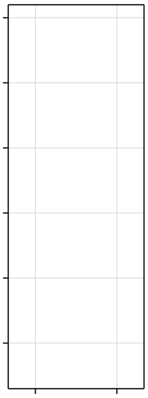

Fig. 17. **(a)** Comparison between the experimental (black solid) and theoretical (blue dashed) P- and S-wave velocities and density of Well 1 by modeling workflow in Fig. 12 for Test 1. **(b)** Anisotropic parameters ε, δ, and γ (blue solid).

Test 6: In this test, the three parameters LI, r_{con}, and α_{con} are inverted. The results are shown in Fig. 22. This test exhibits the smallest error. Fig. 22(b) shows that the P-wave anisotropy parameter ε ranges from 0.19 to 0.44 and the S-wave anisotropy parameter γ ranges from 0.15 to 0.49, indicating a strong anisotropy.

To more clearly illustrate the advantages of the proposed modeling scheme, we present the predicted results of the six tests mentioned above in an overlapped display, as shown in Fig. 23. Combined with Table 3, it can be seen that the rock physics model corrected using the inverted three parameters (LI, r_{con} and α_{con}) in Test 6 yields the highest prediction accuracy. The model considering two inverted parameters (Test 5) has the next highest accuracy of the predicted results. In contrast, models that only consider a single parameter (Tests 2–4) show a noticeable decline in accuracy, while the condition where all three parameters are set as constants (Test 1) results in the highest prediction errors. These findings highlight that when developing a rock physics model, incorporating more sensitive auxiliary parameters may lead to greater model accuracy. However, this conclusion still requires further verification with actual measured data. At the same time, it is important to account for the ill-posedness of the inverse problem. Additionally, the predicted density remains the same in all tests, as we have assumed that density is unaffected by pore structure or clay-kerogen lamination during modeling.

Table 3
Relative root mean square errors (RRMSE) and correlation coefficients (CC) between the experimental and theoretical velocities corresponding to the different tests.

Test	RRMSE		CC	
	V_{P}	V_{S}	V_{P}	V_{S}
1	4.7070	4.1225	0.7727	0.7165
2	3.8577	2.6047	0.8296	0.8584
3	3.1089	2.7375	0.8491	0.8669
4	3.6102	2.0577	0.8034	0.8870
5	2.4023	1.5554	0.8920	0.9278
6	1.2381	0.8109	0.9772	0.9885

5. Application

Pre-stack seismic inversion is a key technique for extracting reservoir elastic properties and anisotropic information from pre-stack gathers. Estimating anisotropy parameters by inversions provides essential data for sweet spot prediction in shale reservoirs. However, in practice, obtaining anisotropic parameters can

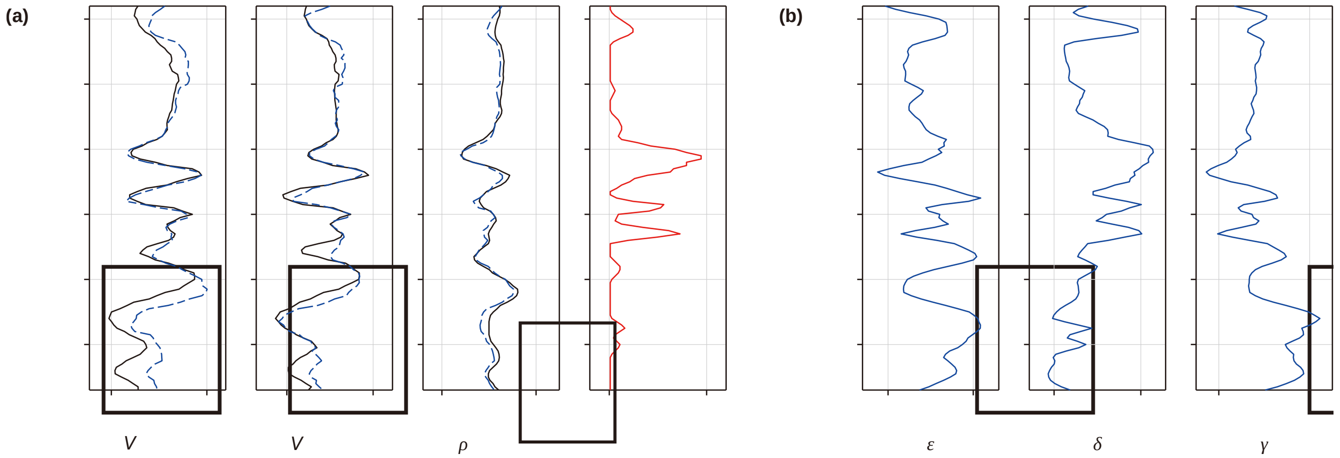

Fig. 18. **(a)** Comparison between the experimental (black solid) and theoretical (blue dashed) P- and S-wave velocities and density of Well 1 by modeling workflow in Fig. 12 for Test 2. **(b)** Anisotropic parameters ε, δ, and γ (blue solid).

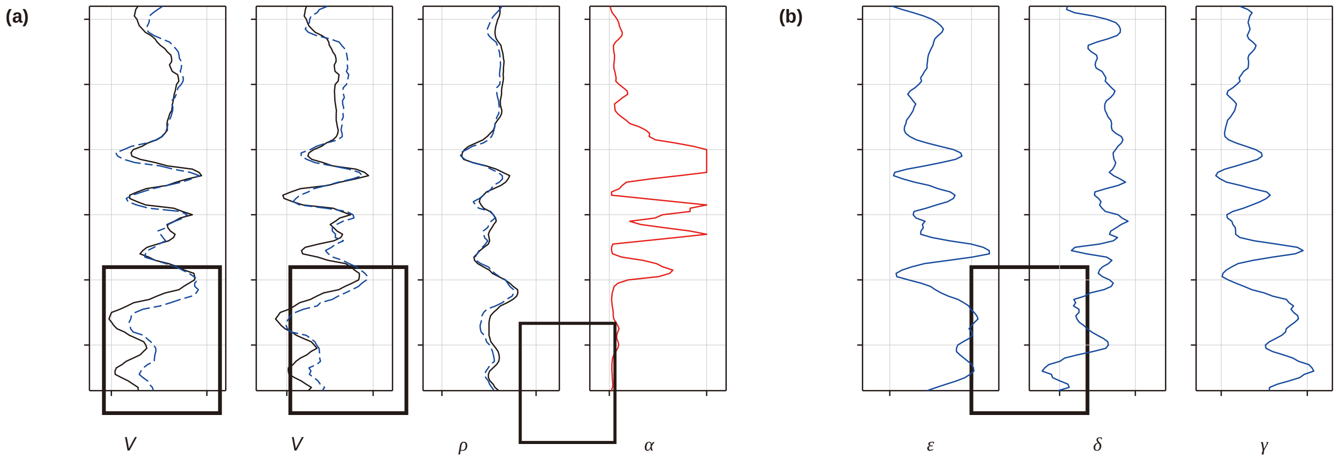

Fig. 19. **(a)** Comparison between the experimental (black solid) and theoretical (blue dashed) P- and S-wave velocities and density of well 1 by modeling workflow in Fig. 12 for Test 3. **(b)** Anisotropic parameters ε, δ, and γ (blue solid).

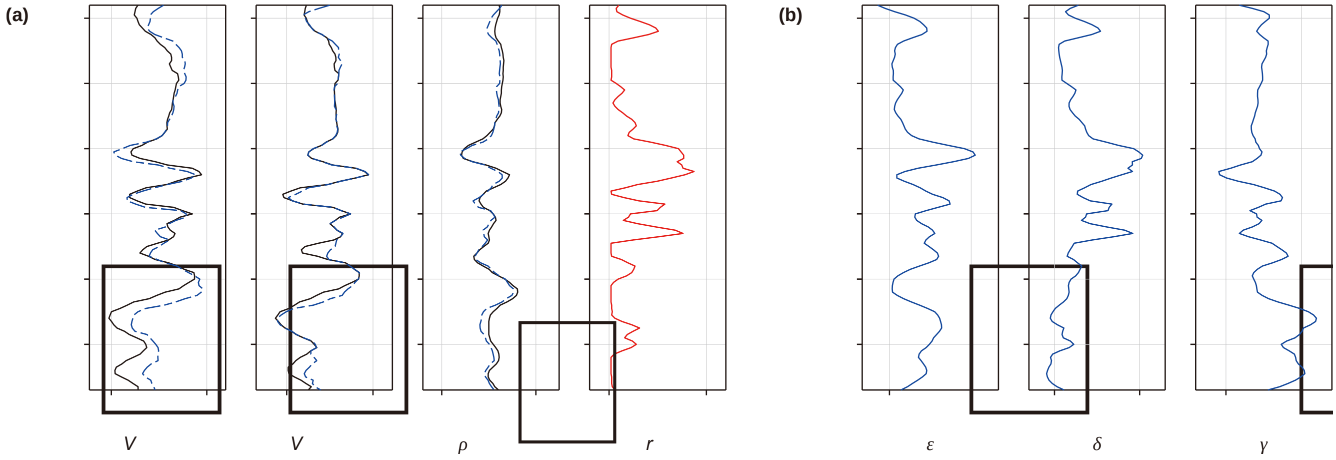

Fig. 20. **(a)** Comparison between the experimental (black solid) and theoretical (blue dashed) P- and S-wave velocities and density of Well 1 by modeling workflow in Fig. 12 for Test 4. **(b)** Anisotropic parameters ε, δ, and γ (blue solid).

be challenging, as many well logs do not include these parameters, making model-based inversion techniques difficult to apply. The modeling approach proposed in this study allows for estimating the elastic and anisotropic parameters of shale rocks, providing valuable prior information and initial models for subsequent inversion processes.

We conducted application tests using field data from the Sichuan Basin in Southwest China where the reservoir consists of stable shale layers. There is a well penetrating the shale formation with a depth ranging from 3530 to 3900 m at CDP 751. Fig. 24 shows the logging data of Well 2, including the P-wave velocity (V_P), S-wave velocity (V_S), density (ρ), porosity (ϕ), water saturation (S_w), and the mineral components (fraction). The shale formation includes brittle minerals, e.g. quartz, calcite, and pyrite, and a relatively high volume of clay and Kerogen. The shale reservoirs that host shale gas are located at depths ranging from 3740 to 3890 m, characterized by low density, high porosity, and high organic matter content.

Since the anisotropy parameters ε, δ, and γ are not measured directly in the boreholes, we predict them for the shale formation using the proposed modeling approach. Similar to Well 1 in Section 4.2, we performed five tests to verify the effectiveness of the proposed inversion-aided modeling approach. Similar to the test for Well 1, in five tests, all values except for the parameters being inverted are fixed and remain the same across each test case, ensuring the reliability of the test results. The details of the tests are as follows:

(1) Test 1: set LI, r_{con}, and α_{con} constant;
(2) Test 2: invert LI with r_{con} and α_{con} constant;
(3) Test 3: invert α_{con} with LI and r_{con} constant;
(4) Test 4: invert r_{con} with LI and α_{con} constant;
(5) Test 5: invert LI, r_{con}, and α_{con}.

Test 1: We set LI = 10, $r_{con} = 0.6$, and $\alpha_{con} = 0.6$ to predict the elastic properties of the shale formation. The predicted results for P- and S-wave velocities, density, and anisotropic parameters are shown in Fig. 25. As can be seen, the errors in the velocity results are quite apparent.

Test 2: In this test, LI is allowed to vary with depth, and obtained by the inversion method, while r_{con} and α_{con} remain fixed at 0.6. The predicted elastic and anisotropic parameters are shown in Fig. 26. Test 3: This test considers the inversion of α_{con} to account for its variation with depth, with LI = 10 and $r_{con} = 0.6$, the corresponding predicted results are presented in Fig. 27. Test 4: This test incorporates the variation of r_{con} with depth, computed by the inversion method, with LI = 10 and $\alpha_{con} = 0.6$. The prediction results for this test are shown in Fig. 28. Compared to Test 1, the

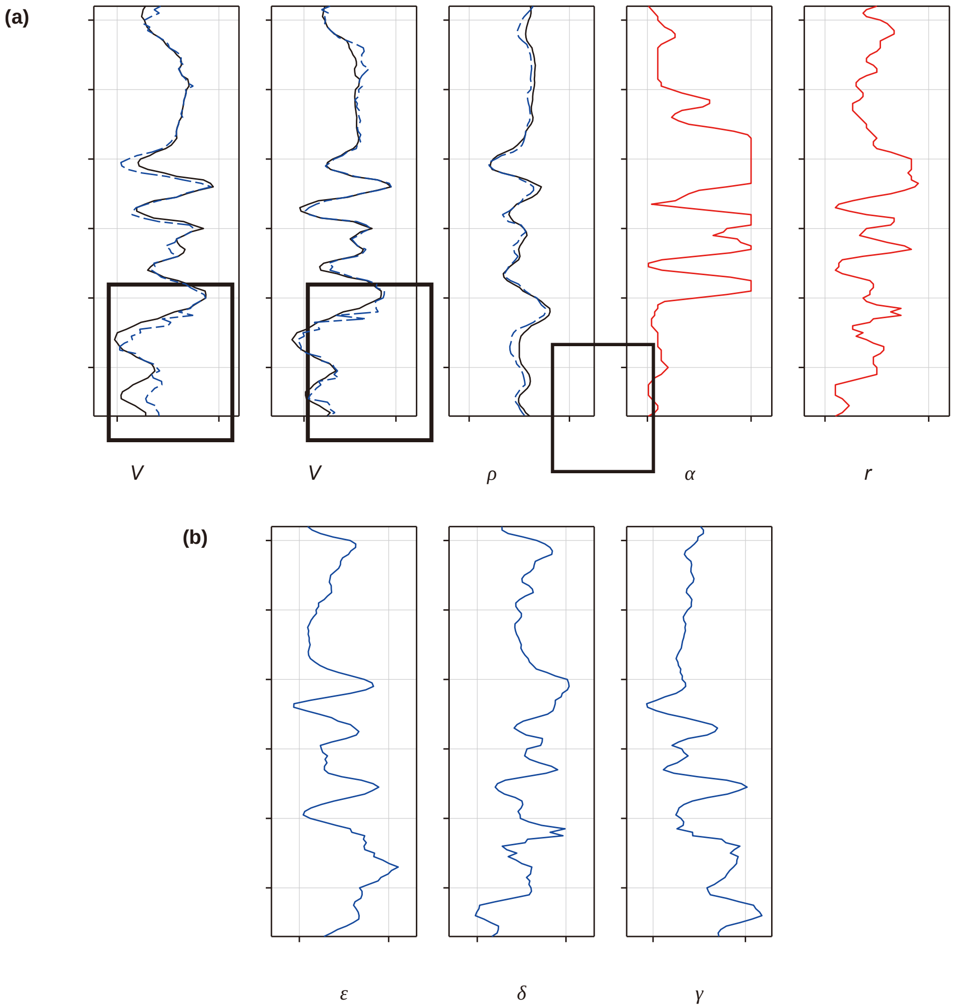

Fig. 21. **(a)** Comparison between the experimental (black solid) and theoretical (blue dashed) P- and S-wave velocities and density of Well 1 by modeling workflow in Fig. 12 for Test 5. **(b)** Anisotropic parameters , δ, and γ (blue solid).

errors of the velocity predictions in Tests 2 to 4 are significantly reduced, but they still show some deviation from the actual values.

Test 5: In this test, LI, α_{con}, and r_{con} are all inverted to vary with depth. The corresponding prediction results are shown in Fig. 29. It can be seen that this test yields the highest prediction accuracy for velocities, with minimal errors compared to the well log measurements. The reservoir section (3740–3890 m) exhibits higher anisotropic parameter values, while the non-reservoir section shows lower values. This aligns with our geological understanding and further validates the feasibility of this modeling method.

In conventional seismic inversion, anisotropic parameters at the well location are typically required to construct initial models and provide prior information, ensuring the proper execution of subsequent seismic AVO inversion. However, in practical applications, measured anisotropic parameters are often not available. To address this issue, we propose an inversion-based rock physics modeling approach to simulate the elastic properties of shale rocks and estimate the anisotropic parameters (shown in Fig. 29(b)), which serve as a critical foundation to ensure the successful implementation of subsequent seismic prestack inversion.

The inversion test was conducted using a set of 2D seismic data crossing the Well 2, covering 141 CDPs with the test well located at CDP 751. Fig. 30 presents the post-stack seismic profile, in which the red curves mark the top and base boundaries of the shale reservoir. The input angle gather of the PP-wave, ranging from 1° to 30°, was divided into three partial stacked sections to enhance the signal-to-noise ratio, with angle intervals of 1°–10°, 11°–20°, and 21°–30°. The angle-dependent wavelets for inversion are estimated from the seismic gathers.

Our inversion methodology employs a simultaneous five-parameter inversion for VTI media based on the Rüger reflection coefficient approximation (Luo et al., 2020, 2021), enabling the estimation of P-wave velocity, S-wave velocity, density, and anisotropy parameters (and δ) in shale formation. Fig. 31 presents the initial models for inversion derived from the estimated elastic and anisotropy parameters in Fig. 29(b), including the models of P- and S-wave velocities, density, and two anisotropy parameters, respectively. During this process, high-frequency information was filtered out, retaining only the essential low-frequency trends. The Rüger-based VTI inversion was then performed, with results of five parameters shown in Fig. 32. It can be observed that the high values of the anisotropy parameters correspond to the shale reservoir locations. The 2D inversion profiles of these anisotropy parameters effectively depict the spatial distribution of the reservoir.

Fig. 33 presents the inversion results from adjacent seismic gathers at the well location, with the black curves representing the rock physics modeling predictions, considered as the ground truth. The blue dashed and red solid curves correspond to the initial model and inversion results, respectively. It demonstrates that

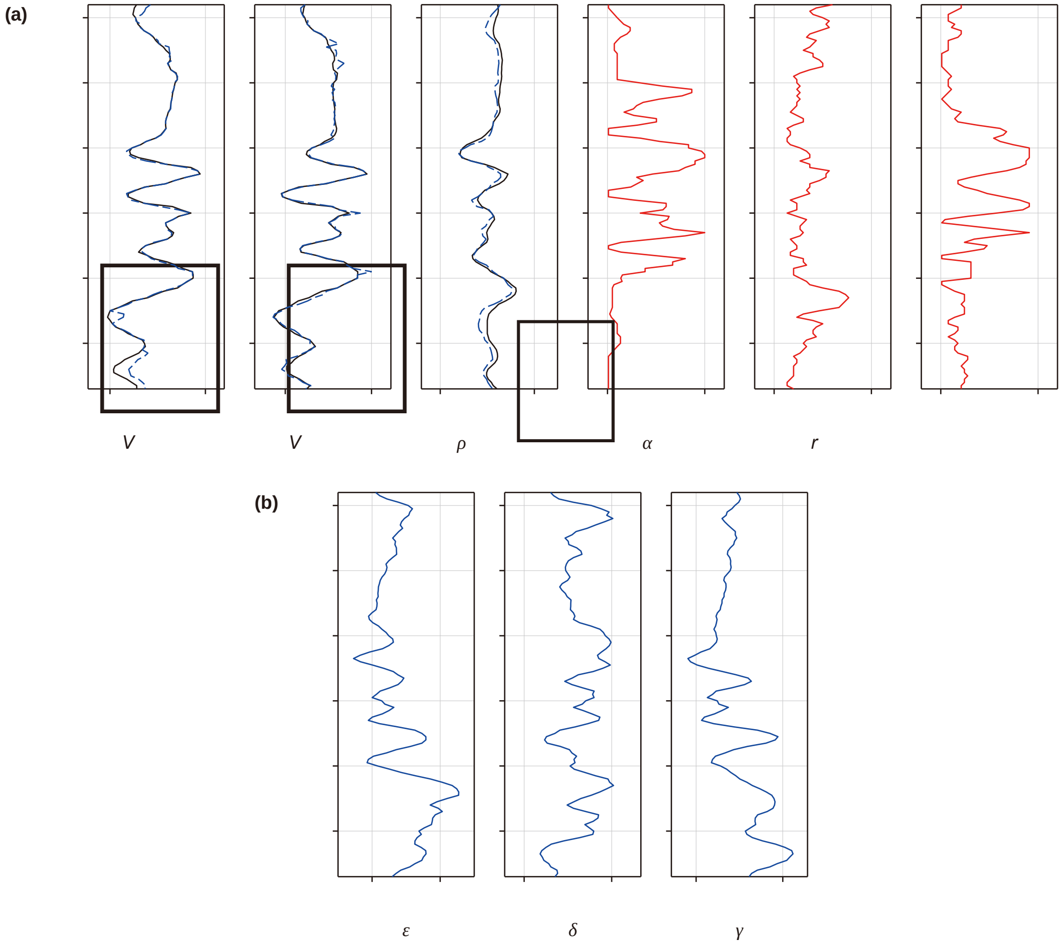

Fig. 22. (**a**) Comparison between the experimental (black solid) and theoretical (blue dashed) P- and S-wave velocities and density of well 1 by modeling workflow in Fig. 12 for Test 6. (**b**) Anisotropic parameters ε, δ, and γ (blue solid).

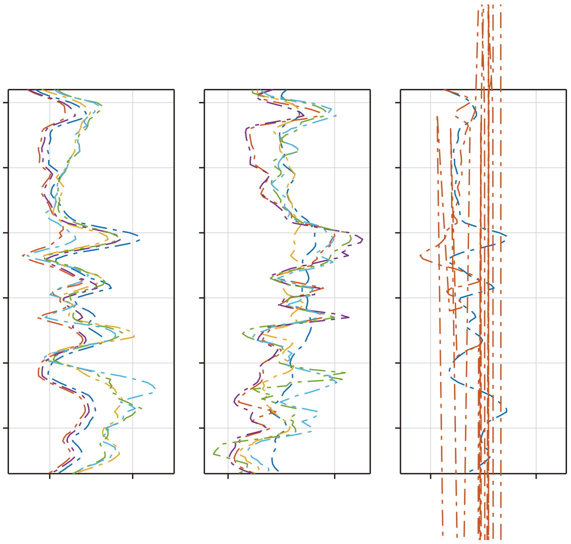

Fig. 23. (**a**) Comparison between the theoretical P- and S-wave velocities and density (colored dashed) of all six tests of well 1 (Figs. 17–22) with the corresponding experimental values (black solid). (**b**) Anisotropic parameters ε, δ, and γ (colored dashed) of all six tests (Figs. 17–22).

velocity and density results exhibit higher accuracy compared to the anisotropic parameters, due to the differing sensitivities of these parameters to seismic data (Luo et al., 2020, 2022). Although the anisotropic parameter estimates show relatively higher errors, they still offer valuable indications of the shale reservoir, providing important information for subsequent sweet spot identification.

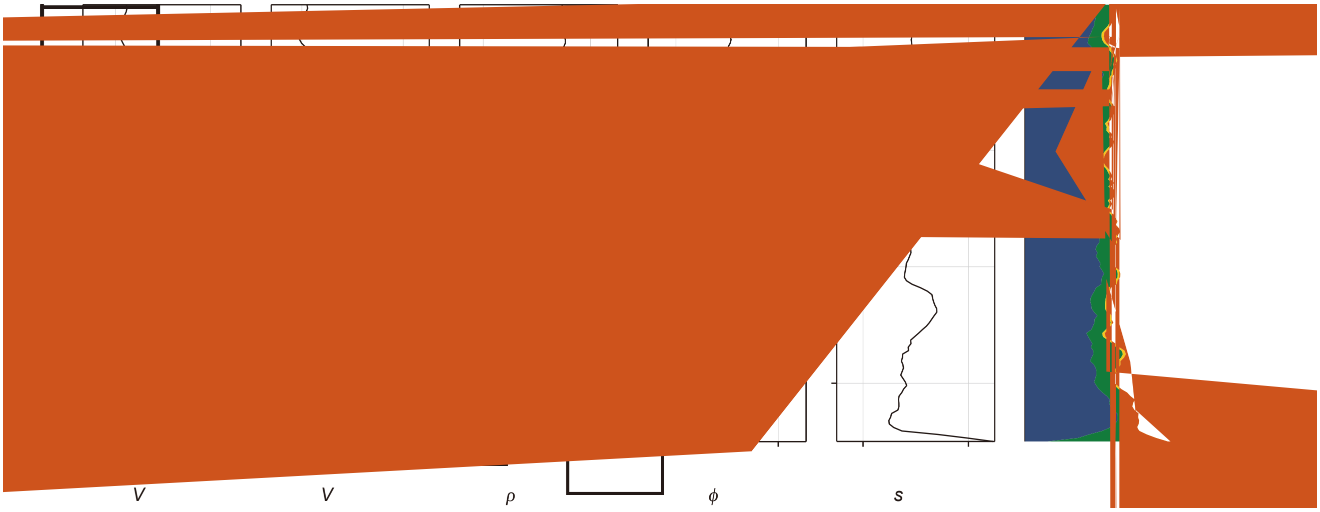

Fig. 24. The logging data of Well 2 including P- and S-wave velocities, density, porosity, water saturation, and mineral fractions.

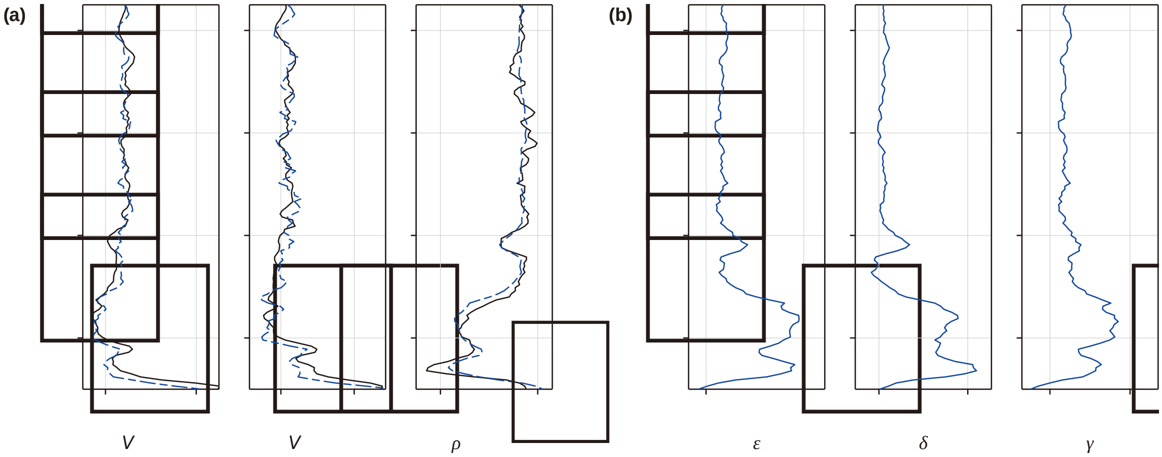

Fig. 25. **(a)** Comparison between the experimental (black solid) and theoretical (blue dashed) P- and S-wave velocities and density of well 2 by modeling workflow in Fig. 12 for Test 1. **(b)** Anisotropic parameters ε, δ, and γ (blue solid).

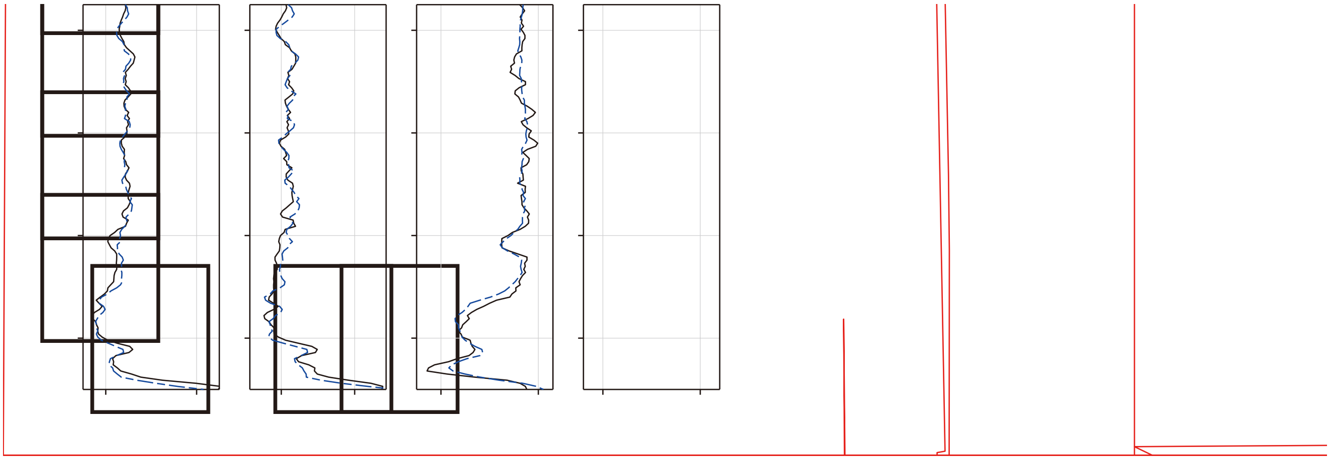

Fig. 26. **(a)** Comparison between the experimental (black solid) and theoretical (blue dashed) P- and S-wave velocities and density of well 2 by modeling workflow in Fig. 12 for Test 2. **(b)** Anisotropic parameters ε, δ, and γ (blue solid).

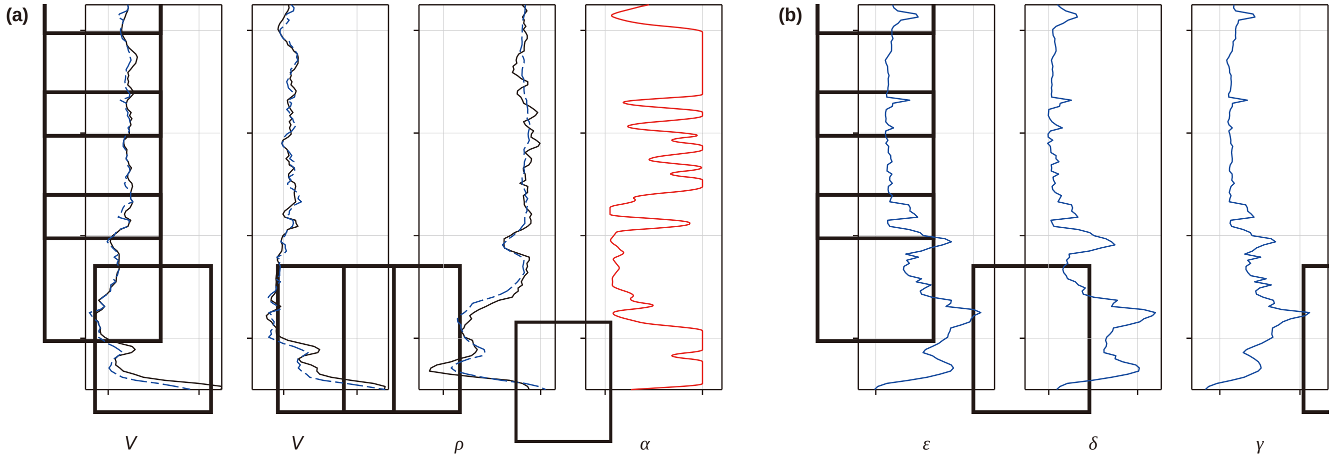

Fig. 27. (**a**) Comparison between the experimental (black solid) and theoretical (blue dashed) P- and S-wave velocities and density of well 2 by modeling workflow in Fig. 12 for Test 3. (**b**) Anisotropic parameters ε, δ, and γ (blue solid).

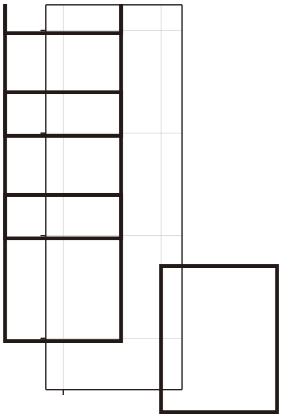

Fig. 28. (**a**) Comparison between the experimental (black solid) and theoretical (blue dashed) P- and S-wave velocities and density of well 2 by modeling workflow in Fig. 12 for Test 4. (**b**) Anisotropic parameters ε, δ, and γ (blue solid).

6. Discussion

Shale exhibits VTI anisotropic characteristics and complex pore structures. In rock physics modeling, it is crucial to account for a variety of influencing factors - including the causes of shale anisotropy and the impact of pores - in order to enhance modeling accuracy. During the modeling process, we simulate the VTI characteristics of shale by considering clay-kerogen lamination and isolated flat pores. In terms of pore structure, we consider the influence of pore shape (aspect ratio), connectivity and distribution on elastic properties.

Fluid flow and solute migration in rocks are macroscopic results of pore structure, which combines both geometric shape (such as pore size and shape) (Bear, 2013) and topological structure (such as pore connectivity) (Dullien, 2012). In particular, when pore connectivity is low, topological factors become more significant than geometric factors (Ewing and Horton, 2002; Hu et al., 2012; Hunt et al., 2014). Therefore, the pore connectivity of shale is an important factor that should be considered. Hu et al. (2015) show that pore connectivity may serve as a dominant constraint on diffusion-limited hydrocarbon transport. Zhao et al. (2023) evaluated the pore connectivity of shale reservoirs using MICP experiments, which showed that a higher proportion of connected pores was observed in the deep shale samples, compared to those in the medium depth. Fu et al. (2019) and Sun et al. (2020) divided pores of shale rocks into connected pores and non-connected pores according to whether it is beneficial to hydrocarbon migration. Dong et al. (2023) pointed that pore size is an important factor influencing oil/gas migration, and classify pores into connected and isolated pores based on different sizes.

In summary, pores in shale exhibit different connectivity, including connected and isolated pores. In previous studies, the

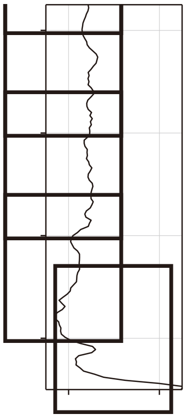

Fig. 29. (**a**) Comparison between the experimental (black solid) and theoretical (blue dashed) P- and S-wave velocities and density of well 2 by modeling workflow in Fig. 12 for Test 6. (**b**) Anisotropic parameters , δ, and γ (blue solid).

definition of whether pores are connected or not is mostly based on the migration of hydrocarbons in shale. Therefore, in this paper, we refer to pores where fluid can migrate as connected pores (corresponding the pores that are interconnected in Fig. 15(b)), and pores where fluid is present as isolated pores (corresponding the pores that are not connected in Fig. 15(a)).

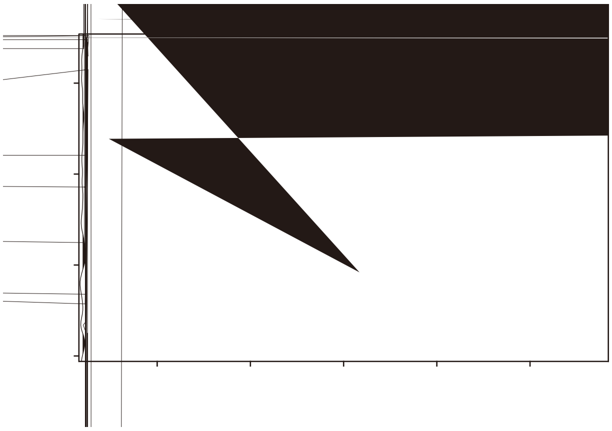

Fig. 30. Seismic post-stack profile through the Well 2 at CDP 751, with the red curves highlighting the top and bottom of the shale reservoir.

In the modeling test, we set all parameters to remain unchanged except for the parameters to be inverted in each test, in order to ensure the validity of the conclusions. Therefore, the size of the errors between the predicted and measured velocities in tests can, to some extent, reflect the accuracy of the forward model. However, a good data fit does not necessarily indicate that the model is accurate. The most reliable way to validate the model is by comparing it with the measured anisotropic parameters. Due to limitations in the available data, this is not currently feasible. The lack of the measured anisotropy parameters is, in fact, the main motivation behind the modeling in this work: to provide reference anisotropy parameter estimations for subsequent anisotropy inversion and seismic prediction in shale reservoirs, especially when measured data is limited. This proposed modeling approach will undergo further validation and refinement in our future work.

For the tests on different wells, the estimated values of LI, r_{con}, and α_{con} are set within the same search range. This is because these parameters cannot be directly measured, and we lack prior information to define their specific range at different well locations. As a result, the search range we provide includes all possible values of these parameters. However, to mitigate the ill-posedness of the inversion and improve efficiency, we have restricted the numerical ranges based on the physical meaning of the parameters, such as limiting the range of r_{con} and α_{con} to [0, 1]. The LI range is set to [0, 100], as our sensitivity analysis shows that when LI exceeds 100, the changes in elastic and anisotropic parameters become negligible (see Figs. 10 and 11). Therefore, we consider that the numerical range of [0, 100] to be sufficient for our purposes.

Additionally, we have focused sole LI

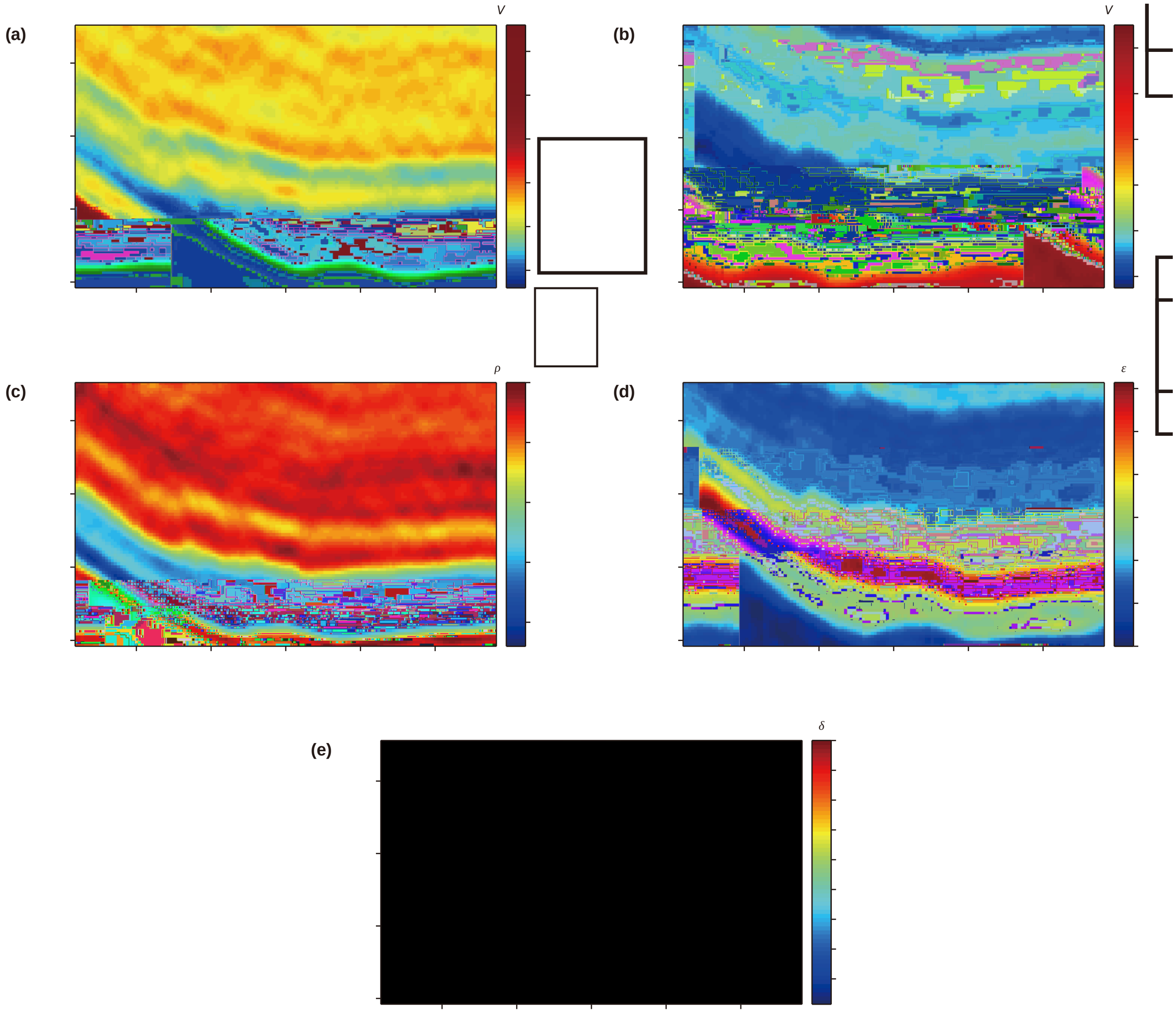

Fig. 32. The results by the Rüger-based prestack simultaneous inversion, including **(a)** P-wave velocity, **(b)** S-wave velocity, **(c)** density, anisotropy parameters **(d)** -and **(e)** δ.

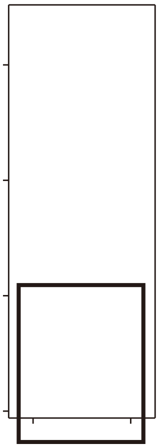

Fig. 33. The results at the well location obtained with the Rüger-based prestack simultaneous inversion. The black solid lines are the real logs, and the blue dotted and red curves are the initial logs and inversion results, respectively.

subsequent seismic inversion has low dependence on additional parameters and offers high applicability.

7. Conclusions

To estimate the elastic and anisotropy parameters of source rocks (shale), an inversion approach supported by rock physics modeling is proposed, combining inclusion-based models (SCA and DEM) with the Brown-Korringa equations. To model pore complexity, we introduce a connectivity index to quantify the effects of the two pore types (connected and isolated) and use aspect ratios to describe the pore geometries. The effective anisotropy of the shale is described with oriented clay-kerogen platelets and isolated microcracks based on a lamination index.

First, we perform a sensitivity analysis by varying the lamination index, the orientation angle of the platelets, the connectivity and isolation indices, and the aspect ratios of the two types of pores (connected and isolated) to estimate the effects on the elastic properties of the shale. It is shown that the lamination index and the connected pores have a more significant influence.

Subsequently, the lamination and pore connectivity indices as well as the aspect ratio of the connected pores are treated as unknown parameters and inverted from the experimental (log) vertical P- and S-wave velocities by a simulated annealing algorithm. To verify the effectiveness of the proposed inversion approach, six tests are performed on Well 1, tests 1 to 5 based on fixing some of the parameters. Test 6, which is based on the inversion of the three parameters, shows the best accuracy. The test results of the other well (Well 2) yield the similar conclusion. The elastic and anisotropic parameters predicted using the proposed modeling method were applied in pre-stack seismic VTI inversion for shale formations. Seismic applications demonstrate that our shale modeling approach provides important data support for establishing the initial model for subsequent inversions.

CRediT authorship contribution statement

Cong Luo: Methodology, Formal analysis, Writing – original draft, Funding acquisition, Conceptualization. **Jun-Wei Cheng:** Visualization, Formal analysis, Writing – original draft, Methodology. **Jing Ba:** Supervision, Conceptualization, Writing – review & editing, Resources. **José-Maria Carcione:** Writing – review & editing, Conceptualization, Supervision. **Lu-Lu Chen:** Writing – original draft, Visualization.

Declaration of competing interest

The authors declare that they have no known competing financial interests or personal relationships that could have appeared to influence the work reported in this paper.

Acknowledgements

This work was funded by the National Natural Science Foundation of China (No. 42374128) and by the Fundamental Research Funds for the Central Universities (No. B240201110).

Appendix A. Self-consistent approximation (SCA)

Berryman (1980) proposed the self-consistent approximation (SCA), a method for computing the elastic modulus of a model composed of multiphase minerals and pores. It treats each mineral component and pore space as an independent single phase. SCA is a "symmetric" effective theory that treats each component equally (there is no defined background medium). The isotropic SCA model can be expressed as

$$\sum_{i=1}^{n} x_i (K_i - K^*) P^{*i} = 0, \tag{A-1}$$

$$\sum_{i=1}^{n} x_i (\mu_i - \mu^*) Q^{*i} = 0, \tag{A-2}$$

where i refers to the ith component (mineral or pore), with volume fraction x_i, K_i and μ_i are the bulk and shear moduli, respectively, and P and Q define the shape of the inclusions, on the basis of the pore aspect ratio α.

The SCA can be extended to the case of anisotropy (Hornby et al., 1994):

$$\begin{aligned} \tilde{\mathbf{C}}^{\mathrm{eff}} = {} & \sum_{n=1}^{N} v_n \tilde{\mathbf{C}}^{n} \left(\mathbf{I}_{\mathrm{ijkl}} + \tilde{\mathbf{G}}_{\mathrm{ijkl}} \left(\tilde{\mathbf{C}}^{n} - \tilde{\mathbf{C}}^{\mathrm{eff}} \right) \right)^{-1} \\ & \left\{ \sum_{p=1}^{N} v_p \left(\mathbf{I}_{\mathrm{ijkl}} + \tilde{\mathbf{G}}_{\mathrm{ijkl}} \left(\tilde{\mathbf{C}}^{p} - \tilde{\mathbf{C}}^{\mathrm{eff}} \right) \right)^{-1} \right\}^{-1}, \end{aligned} \tag{A-3}$$

where, $\tilde{\mathbf{G}}_{\mathrm{ijkl}} = (\overline{\mathbf{G}}_{\mathrm{ikjl}} + \overline{\mathbf{G}}_{\mathrm{jkil}})/8\pi$, $\mathbf{G}_{\mathrm{ijkl}}$ is the Eshelby tensor, which defines the shape of each inclusion, $\mathbf{I}$ is the unit tensor, $\tilde{\mathbf{C}}^{n}$ ($\mathbf{C}^{p}$) are the stiffness matrices of the $n(p)$th phase, and $v^{n(p)}$ is the respective volume fraction.

Appendix B. Differential effective medium (DEM)

Differential effective medium (DEM) calculates the properties of multi-phase mixtures by gradually adding inclusion phases into solid minerals. When different background minerals are selected or the order of the added minerals varies, the results are different. The equations of the isotropic DEM model are (Mavko et al., 2009)

$$(1-y)\frac{\mathrm{d}}{\mathrm{d}y}[K$$

Bandyopadhyay, K., 2009. Seismic Anisotropy: Geological Causes and its Implications to Reservoir Geophysics. Stanford University, California, United States. Ph. D thesis.

Bear, J., 2013. Dynamics of Fluids in Porous Media. Courier Corporation, North Chelmsford, Massachusetts.

Berryman, J.G., 1980. Long-wavelength propagation in composite elastic media II. Ellipsoidal inclusions. J. Acoust. Soc. Am. 68 (6), 1820–1831. https://doi.org/10.1121/1.385171.

Bokhonok, O., Ravazzoli, C.L., 2016. The influence of kerogen content on some brittleness indicators in a rich organic shale: comparative analysis of different approaches. In: VII Simposio Brasileiro de Geofísica. SBGF, 201610.

Brown, R.J.S., Korringa, J., 1975. On the dependence of the elastic properties of a porous rock on the compressibility of the pore fluid. Geophys 40 (4), 608–616. https://doi.org/10.1190/1.1440551.

Carcione, J.M., 2000. A model for seismic velocity and attenuation in petroleum source rocks. Geophys 65, 1080–1092. https://doi.org/10.1190/1.1444801.

Carcione, J.M., 2022. Wave Fields

Sarout, J., Guéguen, Y., 2008. Anisotropy of elastic wave velocities in deformed shales: part 2-modeling results. Geophys 73 (5), D91–D103. https://doi.org/10.1190/1.2952745.

Sayers, C.M., 2005. Seismic anisotropy of shales. Geophys. Prospect. 53 (5), 667–676. https://doi.org/10.1111/j.1365-2478.2005.00495.x.

Soeder, D.J., 1988. Porosity and permeability of Eastern Devonian gas shale. SPE Form. Eval. 3 (1), 116–124. https://doi.org/10.2118/15213-PA.

Sondergeld, C.H., Rai, C.S., 2011. Elastic anisotropy of shales. Lead. Edge 30 (3), 324–331. https://doi.org/10.1190/1.3567264.

Sun, M.D., Zhang, L.H., Hu, Q.H., et al., 2020. Multiscale connectivity characterization of marine shales in southern China by fluid intrusion, small-angle neutron scattering (SANS), and FIB-SEM. Mar. Petrol. Geol. 112, 104101. https://doi.org/10.1016/j.marpetgeo.2019.104101Getrightsandcontent.

Tan, M., Mao, K., Song, X., et al., 2015. NMR petrophysical interpretation method of gas shale based on core NMR experiment. J. Petrol. Sci. Eng. 136, 100–111. https://doi.org/10.1016/j.petrol.2015.11.007.

Thomsen, L., 1986. Weak elastic anisotropy. Geophys 51, 1954–1966. https://doi.org/10.1190/1.1442051.

Vernik, L., Landis, C., 1996. Elastic anisotropy of source rocks: implications for hydrocarbon generation and primary migration. AAPG Bull. 80, 531–544. https://doi.org/10.1306/64ED8836-1724-11D7-8645000102C1865D.

Vernik, L., Nur, A., 1992. Ultrasonic velocity and anisotropy of hydrocarbon source rocks. Geophys 57, 727–735. https://doi.org/10.1190/1.1443286.

Wang, H.M., Tang, X.M., 2021. Inversion of dry and saturated P- and S-wave velocities for the pore-aspect-ratio spectrum using a cracked porous medium elastic wave theory. Geophys 86, A57–A62. https://doi.org/10.1190/geo2021-0071.1.

Wang, H., Sun, S.Z., Yang, H., et al., 2011. The influence of pore structure on P- & S-wave velocities in complex carbonate reservoirs with secondary storage space. Pet. Sci. 8, 394–405. https://doi.org/10.1007/s12182-011-0157-6.

Wu, F., Li, J., Chen, X., Geng, W., Tang, W., 2023. Estimation of pore aspect ratio and capillary pressure coefficient to predict S-wave velocity based on rock physics modeling in orthorhombic anisotropic reservoirs. Explor. Geophys. 3, 229–240. https://doi.org/10.1080/08123985.2022.2117602.

Wu, X., Chapman, M., Li, X.Y., et al., 2012. Anisotropic elastic modeling for 7